Department of Physics and Astronomy
University of Heidelberg

Bachelor Thesis in Physics
submitted by

Carolina Reetz

born in Frankenthal/Pfalz (Germany)

December 2019

Reconstruction of the Hadronic Decay of the Ξ^0_c Baryon with the ALICE Detector

–

Investigation of Charm Production and Validation of the KF Particle Package

This Bachelor Thesis has been carried out by Carolina Reetz at the
Physikalisches Institut of the University of Heidelberg
under the supervision of
Prof. Dr. Silvia Masciocchi

Abstract

The quark-gluon plasma is a state of deconfined strongly-interacting matter (quarks and gluons), which is expected to be created in heavy-ion collisions. The study of charmed baryon production in proton-proton collisions is a crucial step on the way of understanding charm hadronisation processes in the presence of a quark-gluon plasma state. The subject of this thesis is the first reconstruction of the hadronic decay of the Ξ_c^0 baryon in proton-proton collisions at $\sqrt{s} = 5.02\,\mathrm{TeV}$ in the ALICE detector at the LHC. It contributes to the investigation of charm baryon production in proton-proton collisions. The complex decay topology includes the decay hyperons Ξ and Λ. Its reconstruction is performed with the KF Particle package which supports the reconstruction of full particle decay chains, exploiting the use of various constrained fits and including the complete treatment of tracking and vertexing uncertainties. It was developed in the context of the CBM experiment at GSI and is now tested with data recorded by ALICE.

Therefore, different selection criteria related to the reconstruction of the Λ and Ξ decays are investigated. The performance of the commonly used pointing angle variable as selection criterion is compared to the χ^2_{topo} variable provided by the KF package.

This study provides the validation of the KF Particle package for the reconstruction of decay topologies in ALICE and its implementation in the ALICE software framework.

Zusammenfassung

Das Quark-Gluonen-Plasma ist ein Zustand ungebundener stark wechselwirkender Materie (Quarks und Gluonen), von dem erwartet wird, dass er in Schwerionenkollisionen erzeugt wird. Die Untersuchung der Produktion von Baryonen mit Charmanteil in Proton-Proton Kollisionen ist ein entscheidender Schritt, um den Prozess der Hadronisierung von Charm-Quarks in einem Quark-Gluonen-Plasma Zustand verstehen zu können.

Das Thema dieser Arbeit ist die erste Rekonstruktion des hadronischen Zerfalls des Ξ_c^0 Baryons in Proton-Proton Kollisionen bei einer Schwerpunktsenergie von $\sqrt{s} = 5.02\,\text{TeV}$. Diese trägt zur Untersuchung der Charm-Baryon-Produktion in Proton-Proton Kollisionen bei. Die komplexe Zerfalls-Topologie beinhaltet die Hyperonen Ξ und Λ. Ihre Rekonstruktion wird mithilfe des KF Particle Pakets durchgeführt, welches die Rekonstruktion vollständiger Teilchenzerfallsketten unterstützt, unter der Verwendung unterschiedlicher einschränkender Fits und vollständiger Rücksichtnahme von Spur- und Vertexunsicherheiten. Es wurde im Kontext des CBM Experimentes am GSI entwickelt und wird jetzt an Daten getestet, die mit dem ALICE Detektor aufgenommen wurden.

Dazu werden verschiedene Selektionskriterien, die mit der Rekonstruktion der Λ und Ξ Zerfälle verbunden sind, untersucht. Das Verhalten der für gewöhnlich verwendeten Pointing Angle Variable als Selektionskriterium wird mit der χ^2_{topo} Variable, die vom KF Paket verwendet wird, verglichen.

Diese Untersuchungen liefern die Validierung des KF Particle Pakets für die Rekonstruktion von Zerfalls-Topologien im ALICE Detektor und dessen Anwendung im ALICE Software-Framework.

Contents

1 Introduction

The entire matter in the visible universe, as we know it today, is composed of a handful of fundamental particles (see Fig. 1.1) called fermions which are grouped in the *Standard Model of particle physics (SM)*. These matter particles exist in three generations with increasing mass and they are either quarks or leptons. For every fermion there exists an associated antiparticle with the same mass but opposite charge. The SM includes three types of interactions between these fundamental particles: the strong, the electromagnetic, and the weak interaction, mediated by the so called *gauge bosons*. The gravitational force is the fourth fundamental interaction between all massive particles. Its integration into the SM is one of the greatest challenges in today's physics.

The strong interaction, which is responsible for the binding force between quarks, is described by a relativistic quantum field theory referred to as *quantum chromodynamics (QCD)*. QCD describes quarks as the fundamental constituents of matter which come in six different flavours and carry mass, spin, and electric charge as well as one of three colour charges (or three anticolours) and form colour neutral observable particles. The mediators of the strong force, the 8 types of massless coloured gluons, couple to couloured quarks, antiquarks, and other gluons by exchanging colour.
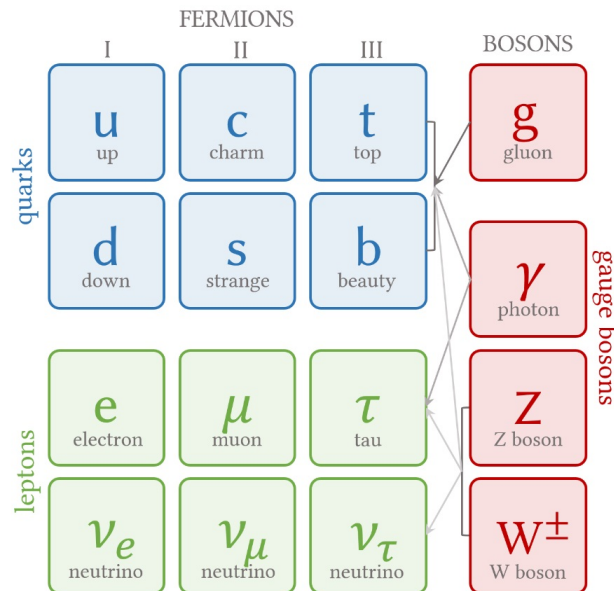

Figure 1.1: Particles in the Standard Model of particle physics (figure inspired by [1]).
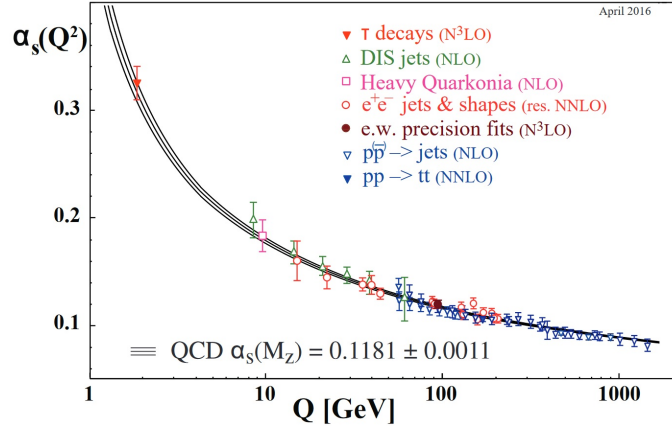
Figure 1.2: Strong coupling constant α_s as a function of the momentum transfer Q in a collision of quarks and/or gluons[2].

The potential V(r) of the strong interaction between two quarks is described as follows:

$$V(r) = -\frac{4}{3}(\hbar c)\frac{\alpha_s}{r} + kr \qquad (1.1)$$

where r is the distance between the two quarks, α_s the coupling constant of the strong interaction, k the "spring constant", $\hbar$ the reduced Planck constant, and c the speed of light. This potential indicates two fundamental principles of QCD: the *asymptotic freedom* at small (large) and the *colour confinement* at large (small) distances (momentum transfer Q^2). The potential is weak for small distances, hence, in this regime the quarks exist quasi-freely. This gives rise to the fact that the value of the strong coupling constant α_s varies with the amount of energy transfer as shown in Fig. 1.2. α_s is calculated to be [3]:

$$\alpha_s(Q^2) = \frac{12\pi}{(33 - 2n_f)\ln Q^2/\Lambda_{QCD}^2} \qquad (1.2)$$

where n_f is the number of quark flavours. Due to the *running* of the coupling, for high momentum regimes, where $Q^2 \gg \Lambda_{QCD}^2$ with the scale factor $\Lambda_{QCD} \approx 200\,\text{MeV}$ [3], perturbative Quantum Chromodynamics (pQCD) calculations are applicable.

Since the strong potential rises with increasing distance between the particles, it is impossible to separate two quarks from each other. This is a consequence of the coupling diverging for momentum transfers equal to Λ_{QCD}. As a result, quarks only exist confined in *hadrons* and have never been measured freely. We either observe combinations of three quarks, called *baryons*, or pairs of a quark and an antiquark which are referred to as *mesons*.
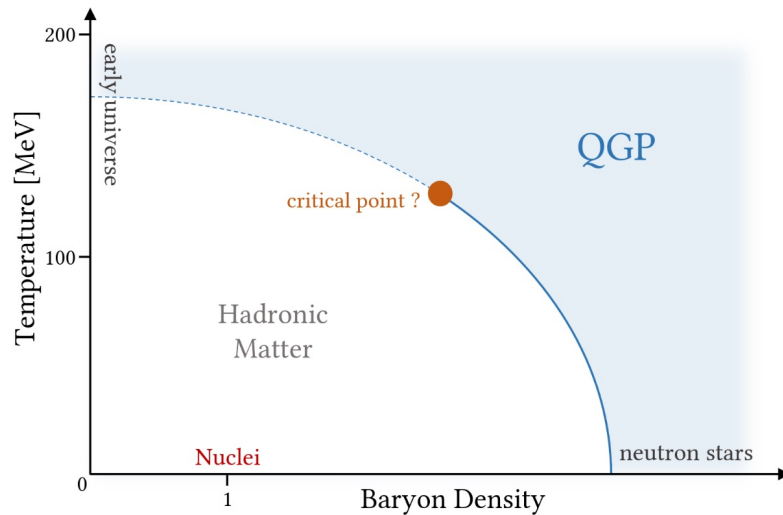
Figure 1.3: The QCD phase diagram. The baryon density is normalised to the nuclei baryon density (figure inspired by [4]).

1.1 Heavy-Ion Collisions and the Early Universe

In its very early stages the universe was in a state of extremely high temperature and energy density.

In heavy-ion (HI) collisions, where high densities of matter are reached, hadrons begin to interpenetrate each other and the participating quarks rather move on a distance corresponding to the size of a nuclei than to the size of a hadron. This state of matter, in which quarks and gluons can be considered free, is called *quark-gluon plasma (QGP)*. The QGP is expected to be at the inner core of neutron stars, which are very cold but also the most dense objects in our universe. At high temperatures, as in the early universe, the same state of matter is produced. Both, neutron stars and the early universe, are not directly accessible for measurements Therefore, the QGP is investigated in HI collisions where high temperatures and energy densities are reached.

1.1.1 The Quark-Gluon Plasma in Heavy-Ion Collisions

The matter surrounding us can exist in different states. Transitions from one phase to another are induced by a change of the external conditions. The asymptotic freedom described in QCD gives rise to the theory of a phase transition between hadronic matter and a medium of QGP. This transition, depending on the change of temperature and baryon density, is described by the phase diagram of QCD in Fig. 1.3. At low temperatures and increasing baryon density the hadronic matter goes through a phase transition

possibly resulting in the QGP state. The transition above the potentially existing critical point of the phase diagram, meaning at low density and increasing temperature, would be rather a smooth cross over than a phase transition. This transition from confinement to deconfinement at high temperatures is expected to be reached in HI collisions.

When heavy ions are brought to collision at rather low energy, the nuclei as a whole interact with each other. With an increase of the collision energy, the nucleons inside the nuclei begin to interact and as a result different particle species are produced. At relativistic energy scales, the quarks inside the nucleons interact during the collision process. In this case, the collision passes through different stages which are depicted in Fig. 1.4.

The two Lorentz contracted nuclei travelling at nearly the speed of light collide at t = 0, z = 0 (see Fig. 1.4). During the partonic interaction, a fireball is created which is a highly excited state expanding in spacetime. In the pre-equilibrium stage, the constituents of the fireball collide to reach local thermal equilibrium and after the time $\tau_{\mathrm{QGP}} \approx 0.3 - 1.5\,\mathrm{fm/c}$ QGP is formed where the quarks and gluons are no longer confined but move freely in the medium. This thermalised state undergoes expansion, meaning that the energy density decreases and the system cools down until it reaches the critical temperature $\mathrm{T}_{\mathrm{cr}} \approx 155\,\mathrm{MeV}$ or rather the critical energy density $\epsilon_{\mathrm{cr}} \approx 1\,\mathrm{GeV/fm}^3$ [5]. Below this critical values the partons can no longer exist freely and are confined into hadrons during the hadronisation process. When the system reaches a certain temperature T_{ch}, the inelastic scattering between the produced particles stops and the abundancies of the hadrons are fixed. This is called *chemical freeze-out* which is followed by a further expanding state of the system that is described as *hadron gas*. After some time the mean free path between the constituents of the gas is larger than the range of the strong interaction and the elastic scattering stops. After this so called *kinetic freeze-out* the momentum distributions of the hadrons are fixed and the resulting particles can be detected.

Heavy Flavour

The only observables of the QGP state in HI collisions are the energy and the momentum of the particles created in the collision. In this analysis open heavy-flavour (HF) hadrons containing a heavy quark (charm or beauty) are studied to serve as unique probes of the QGP properties. Due to their mass, which is large compared to the QCD scale factor Λ_{QCD}, heavy quarks are produced in the initial hard scattering processes with large mo-
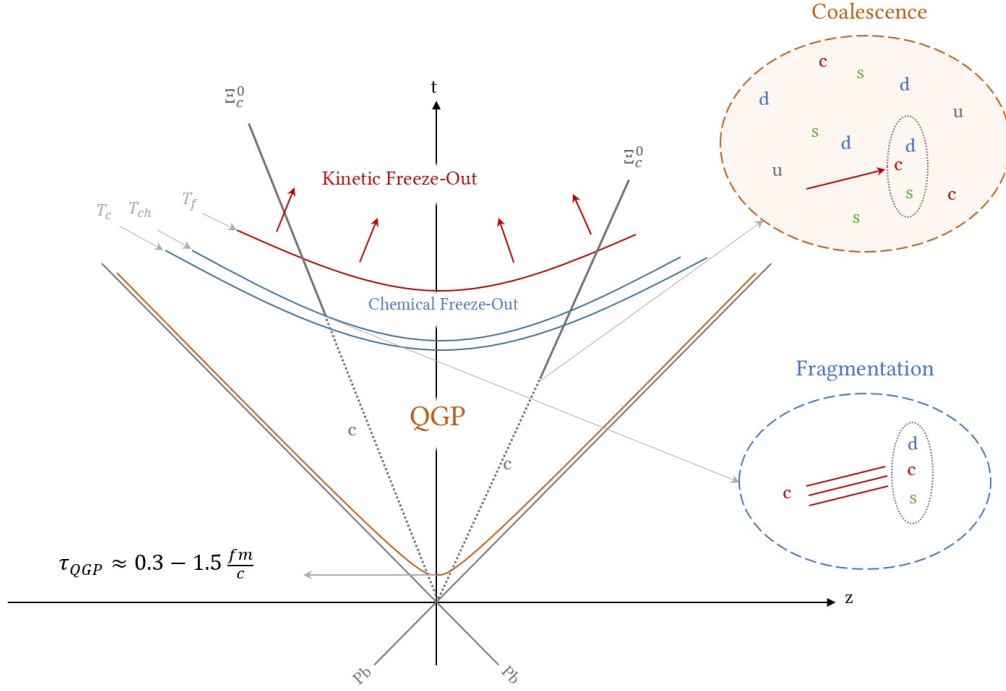
Figure 1.4: Space time evolution of the QGP in HI collisions with two models of the hadronisation process using the example of the Ξ_c^0 baryon (figure inspired by [6]).

mentum tranfer Q^2 on a small generation time scale, which is smaller than the production time τ_{QGP} of the QGP. This leads to the fact that they experience the whole evolution of the QGP interacting strongly with the medium and losing energy while traversing the QGP. All these characteristics make heavy quarks unique probes to study and characterise the QGP.

Hadronisation Processes

One of the main objectives of the study of open HF hadrons is the investigation of the hadronisation mechanism in the freeze-out stage. Although this hadronisation is not fully understood yet, the two following approaches are commonly used to describe it. One model is the *fragmentation mechanism*. If the distance between two quarks is increased, the potential between them rises until the energy reaches a value which is sufficient to produce a new quark-antiquark pair between the two initial quarks. This is a model describing how hadrons are formed from initially "quasi-free" partons combining with other quarks and antiquarks which are spontaneously produced in the vacuum. This process occurs during rapid expansion of the medium and is not influenced by the

QGP.

A second approach to explain how hadrons are formed out of partons is the *quark recombination mechanism*, or *coalescence*, which cannot take place in vacuum. In this scenario, the quark is travelling through the medium, as depicted in Fig. 1.4, losing energy on its way, and picks up a light anti-quark or two quarks with similar momentum, direction, and position as its own and forms a meson or a baryon [7].

The production of heavy-flavour hadrons in proton-proton (pp) collisions is calculated via a factorisation approach. It consists in calculating the transverse momentum (p_T) -differential cross section for the production of HF hadrons as a convolution of the *parton distribution function (PDF)* of the incoming protons, the *parton hard-scattering cross section*, and the *fragmentation function*. The PDF gives the probability to find a parton in the colliding nucleon carrying a certain momentum fraction of this nucleon and it is measured in deep inelastic e^-p scatterings. The partonic cross section is computed by pQCD calculations and represents the probability of the production of heavy quarks. Finally, the fragmentation function describes the probability of heavy quarks to hadronise into a particular hadron and it is assumed to be the same for different collision systems. In order to test this theory, p_T-differential production cross sections of HF hadrons are measured and compared to model calculations based on the factorisation approach.

1.2 Investigations of Charm Baryon Production

The analysis of charm baryons offers a good possibility to investigate the hadronisation process in the presence of QGP and without.

In previous publications [8, 9] the p_T-differential cross sections of charm baryons and the ratio of p_T-differential cross sections for baryons and mesons (baryon-to-meson ratio) were measured in ALICE. Fig. 1.5a shows the average p_T-differential production cross section for $\Lambda_c^+ \rightarrow pK^-\pi^+$, $\Lambda_c^+ \rightarrow pK_s^0$ and $\Lambda_c^+ \rightarrow e^+\nu_e\Lambda$ in pp collisions at $\sqrt{s} = 7\,\text{TeV}$. The same distribution is shown in Fig. 1.5b for $\Lambda_c^+ \rightarrow pK^-\pi^+$ and $\Lambda_c^+ \rightarrow pK_s^0$ in proton-lead (p-Pb) collisions at $\sqrt{s_{NN}} = 5.02\,\text{TeV}$. The measurements are compared to values obtained from theory calculations and in both cases the production cross section is underestimated. In Fig. 1.6 the measured baryon-to-meson ratio for the semi-leptonic decay mode of the Ξ_c^0 baryon and D^0 mesons compared to model expectations based on pQCD calculations and on data from e^+e^- and e^-p collisions is shown. Again, the theory seems to underestimate the ratio of baryons to mesons.

There are two main ideas trying to explain this tension between measurement and the-

Figure 1.5: (a) Λ_c^+ baryon p_T-differential cross section in pp collisions at $\sqrt{s} = 7\,\mathrm{TeV}$ [9] (b) Λ_c^+ baryon p_T-differential cross section in p-Pb collisions at $\sqrt{s_{NN}} = 5.02\,\mathrm{TeV}$ [9].

ory. Hadronisation influences the production of baryons and mesons differently. This could possibly lead to an enhanced baryon production in the presence of QGP. Basically, the formation of a QGP in pp collisions is not expected but since an enhanced baryon-to-meson ratio is also measured in this collision system (Fig. 1.6), it could be an indication for small QGP creation in pp collisions.

Without the creation of a plasma state, the enhanced baryon production in the charm sector could also be explained with *cold matter effects*. Due to a lack of knowledge about the hadronisation of charm into baryonic states, the fragmentation function for this process could be modified in a sense that it is not universal for different collision systems. Therefore, the test of the universality of the fragmentation function is one objective of the charm production measurements.

Now it is also understandable that the investigation of lead-lead (Pb-Pb) and p-Pb as well as pp colliding systems is crucial for a proper understanding of the HF hadronisation process. On the one hand p-Pb and pp measurements are essential as a reference for effects in Pb-Pb collisions, on the other hand it is also necessary to investigate charm baryon production in pp collisions in detail in order to test the predictions of pQCD and to understand the hadronisation process in this collision system.
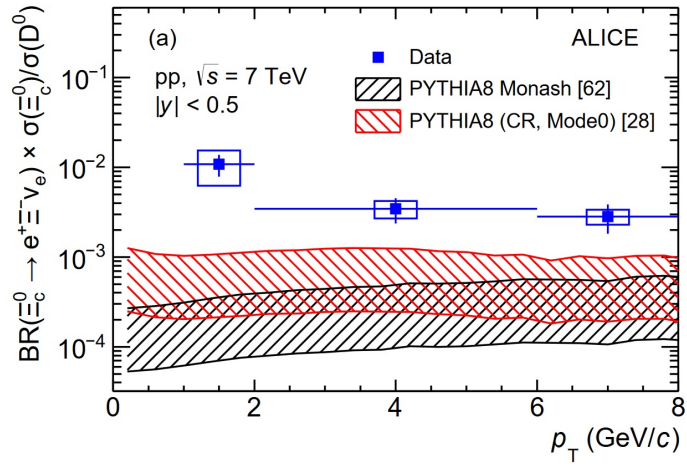
Figure 1.6: Ratio of the p_T-differential cross section of Ξ_c^0 baryons (mulitplied by the branching ratio for the semi-leptonic decay) and D^0 mesons in pp collisions at $\sqrt{s} = 7\,\mathrm{TeV}$ [8].

2 Experimental Apparatus

The study of the behaviour of matter under extremely high temperature values requests high energy-densities such as the ones reached in HI collisions. The *Large Hadron Collider (LHC)* (see Fig. 2.1) at the *European Organisation for Nuclear Research (CERN)* in Geneva is the world's most powerful particle accelerator [10] with a circumference of 26.7 km [11] along which protons as well as heavy nuclei are accelerated in bunches and collided respectively at four different points along the beamline of the accelerator. At each collision point one of the four main experiments of the accelerator complex is located to detect the outcome of the hadron collisions. Apart from the two high luminosity experiments ATLAS and CMS as well as the LHCb detector for the study of beauty physics, the LHC has one experiment dedicated to Pb-Pb ion operation [11] which is called *A Large Ion Collider Experiment (ALICE)*. ALICE is optimised to investigate the
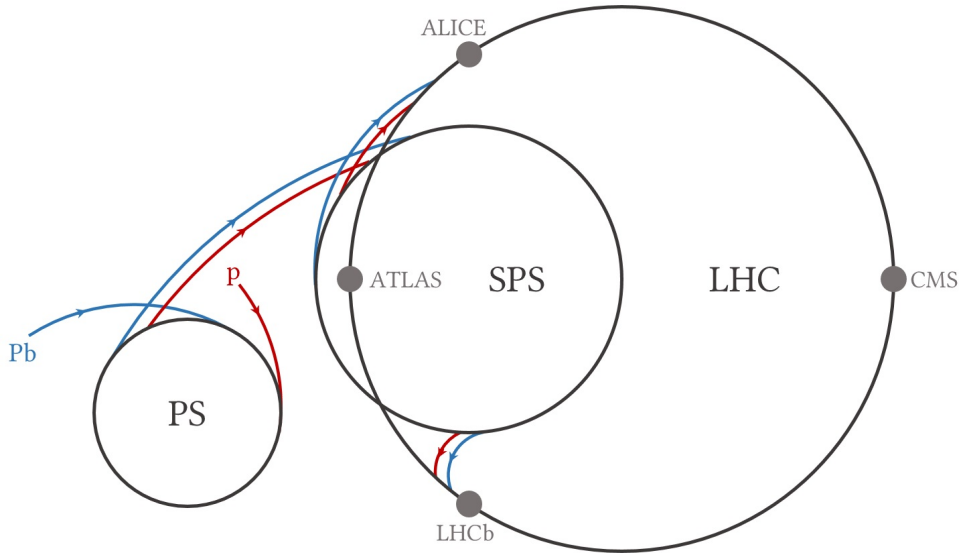

Figure 2.1: The LHC complex with two preaccelerators Proton Synchrotron (PS) and Super Proton Synchrotron (SPS) and the four main detectors. After they have been accelerated in the SPS the hadrons are injected at two different points into separate rings of the LHC resulting in two counter-rotating beams [11] (figure inspired by [12]).

physics of strongly interacting matter and to study and characterise the QGP. In addition to the operation during the lead ions run, the detector also records proton-proton and proton-nucleus collisions.

The data analysed in this thesis originates from pp collisions at a centre-of-mass energy of $\sqrt{s} = 5.02$ TeV measured with the ALICE detector.

2.1 The ALICE Detector

ALICE is designed to be a general-purpose detector measuring a wide range of physics observables. Its overall dimensions cover the size of $16 \times 16 \times 26\,\mathrm{m}^3$ and result in an approximate weight of $10\,000\,\mathrm{t}$ [13]. It consists of 18 different detector systems arranged in a central barrel and surrounded by a large solenoid magnet, which provides a magnetic field with a strength of $0.5\,\mathrm{T}$, and a forward muon spectrometer. Due to this variety of different detector systems it is possible to study hadrons, electrons and photons at midrapidity as well as muons at forward rapidity.

2.1.1 Coordinate System

In order to describe the position of individual detector components and all objects arising from the colliding beams inside the detector, a coordinate system [14] (see Fig. 2.2) is defined for ALICE. It follows the LHC rules which are also used by the other main LHC experiments. The point of origin of the Cartesian coordinate system lies in the centre of the detector denoted as the interaction point (IP) and the z-axis is parallel to the mean beam direction.

The kinematics of a particle of known mass inside the detector are fully described by three independent variables, its momentum in x-y-direction, referred to as transverse momentum p_T, the azimuth angle ϕ and the polar angle θ. Unlike the others, the latter is not Lorentz-invariant along the z-axis. The products of high energy collisions are typically Lorentz boosted along the beam axis which is why θ is replaced by the *rapidity*

$$y = \frac{1}{2} \ln \frac{E + p_z c}{E - p_z c} \tag{2.1}$$

where E is the energy of the particle, p_z its momentum in the longitudinal direction, and c the speed of light. The differences between the rapidities of two particles are invariant with respect to Lorentz boosts along the beam axis (z-axis). For relativistic particles where $E \approx pc \gg mc^2$ the rapidity becomes the so called *pseudorapidity* η,

$$y \approx \eta = -\ln \tan \frac{\theta}{2} \tag{2.2}$$

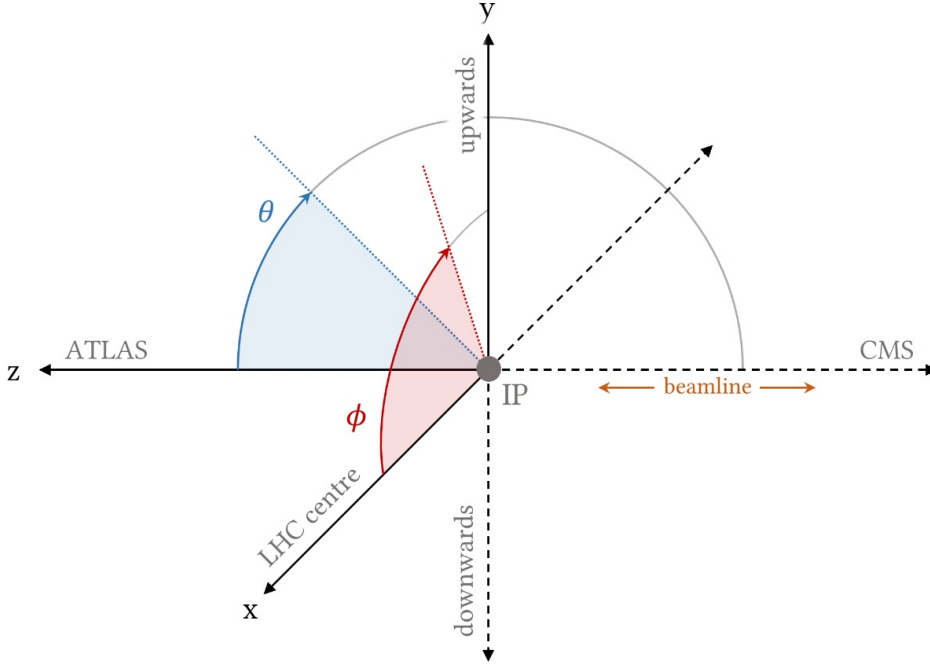which only depends on the polar angle θ.

Figure 2.2: ALICE coordinate system.

2.1.2 ALICE Detector Components

The innermost detectors of the central barrel are the two tracking detectors Inner Tracking System (ITS) and Time Projection Chamber (TPC) which both cover a rapidity range of $|\eta| < 0.9$ [15]. They are surrounded by the Transition Radiation Detector (TRD) ($|\eta| < 0.84$ [13]) used for electron identification for momenta above 1 GeV/c and the Time-Of-Flight (TOF) detector ($|\eta| \lesssim 0.9$ [15]) providing particle identification (PID) of pions, kaons, and protons in the intermediate momentum range. All those detector systems cover the full azimuth around the beam line in contrast to the three outermost detector parts, the High Momentum Particle Identification Detector (HMPID) ($|\eta| < 0.6$ [13]) designed to extend the PID capability, and the two electromagnetic calorimeters Photon Spectrometer (PHOS) ($|\eta| \leqslant 0.12$ [13]) and Electromagnetic Calorimeter (EM-Cal) ($|\eta| \leqslant 0.7$ [13]) with the Di-Jet Calorimeter (DCal) ($|\eta| < 0.7$ [16]).

Furthermore, several other specialised detector systems at different places of the main detector are used for triggering and event characterisation. The VZERO (V0) detector consists of two arrays of scintillator counters, V0A ($2.8 < \eta < 5.1$ [13]) and V0C ($-3.7 < \eta < -1.7$ [13]), on either side of the interaction point (IP) which are used to trigger minimum-bias events and to reject interactions between the beam particles and

the gas in the beam pipe. The minimum-bias trigger consists of the requirement of a coincidence in the two V0 detector components. The two most important detectors used for tracking in this analysis are the ITS and the TPC which are described in detail in the following sections.

Inner Tracking System

The ITS consists of six layers of silicon-detectors arranged cylindrically around the beam pipe, which has an outer diameter of 6 cm [15], and it covers the pseudorapidity range of $|\eta| < 0.9$ for all vertices located within the range of z $= \pm 5.3$ cm [13]. The two innermost layers, referred to as Silicon Pixel Detectors (SPD), operate at a region where the track density in HI collisions can be up to 50 tracks/cm^2 [13]. The SPD plays a major role in the determination of the position of the primary vertex (PV) as well as in the reconstruction of secondary vertices and impact parameters of secondary tracks which is particularly important for measurements of open charm decays. The impact parameter is reconstructed with a resolution better than 60 µm in the azimuthal plane (for $p_T > 1$ GeV/c) [13].

The four outermost detector layers, where a lower particle density is expected, are divided into two Silicon Drift Detectors (SDD) and two Silicon Strip Detectors (SSD) providing, among other things, a measurement of the specific ionisation energy loss which is needed for the PID of low-momentum particles in the ITS.

The main functions of the ITS can be summarised as the localisation of the PV and the improvement of angle and momentum resolution of high-p_T particles by matching their tracks form the TPC to the ITS. The tracking and identification of low-p_T particles whose tracks are curved by the magnetic field of ALICE to such an extent that they will not reach the parts of the detector which are located further away from the PV than the ITS are also one of the major functions.

Time Projection Chamber

The ALICE TPC is a very unique instrument for tracking and for charged particle identification measurements in the high multiplicity enviroment given inside the ALICE detector. It provides important particle tracking capabilities which make it the primary detector for track reconstruction (see Sec. 2.2.1) for the ALICE experiment. The large cylindrical detector with an active volume of about 90 m^3 [18] encloses the ITS and covers the full azimuth around the beamline. It has an inner radius of 85 cm, an outer radius
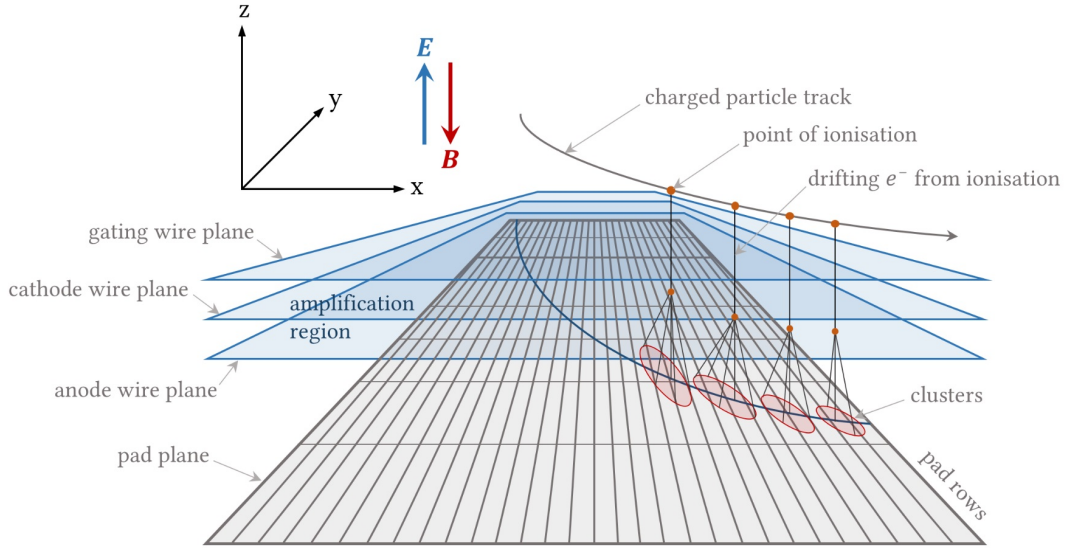
Figure 2.3: Readout Chamber (ROC) showing the principle of the signal amplification by the multi-wire proportional chamber (MWPC) and the forming of clusters in the pad plane. The gate wire is supposed to prevent the ions created in the amplification region to drift back into the interior of the TPC. The centre of gravity of each cluster is later used in the track reconstruction as reconstruction point (figure inspired by [17]).

of 250 cm, and a length of 500 cm along the z-direction [13]. The TPC covers a pseudo-rapidity range of $|\eta| < 0.9$ for tracks with full radial length [13]. The chamber is divided into two parts by a central high voltage electrode providing an electrical potential between the endplate electrodes and itself. The endplates on each side of the chamber are divided into 18 trapezoidal sectors in azimuthal direction and 2 sectors in the radial direction (due to the radial dependence of the track density) resulting in 72 Readout Chambers (ROC) overall. The interior of the TPC is filled with a $NeCO_2N_2$ gas mixture with a small radiation length and low multiple scattering rates.

When a charged particle crosses the gas filled chamber, it ionises the gas molecules on its way and the emerging electrons drift along the electric field towards the endplates with a maximal drift time of $t_D \sim 92\,\mu m$ [13]. At the endplates they induce a signal inside the readout chambers (see Fig. 2.3) which gets amplified by multi-wire proportional chambers (MWPC) and read out via clustering by several readout pads. The readout chambers contain 159 rows of pads along the radial extension and about 560 000 pads overall which means a passing track can maximally induce 159 clusters in the TPC. Due to a limited detector efficiency, there is not in every pad row that a particle crosses a cluster detected. Therefore, the number of crossed rows is defined as the sum of the

number of clusters and the number of pad rows without signal, but with clusters in both adjacent rows. The number of findable clusters is the number of pad rows which are possible clusters based on the geometry of the track.

The position of the initial ionisation by a charged particle in the x-y-plane can be determined by the pad position where the corresponding cluster gets induced, whereas the position in the z-y-plane must be calculated using the total drift time and the drift velocity of the electron arising from the ionsation. This is how the information for a full 3D reconstruction of the tracks is provided.

Charged particle tracks are bent by the magnetic field of the solenoid magnet surrounding the central barrel which allows a good measurement of the momentum of the particle. The mean rate of energy loss by ionisaton of a particle passing through a medium with atomic number Z and mass number A is described by the Bethe-Bloch formula [2]

$$\left\langle -\frac{dE}{dx} \right\rangle = K z^2 \frac{Z}{A} \frac{1}{\beta^2} \left[\frac{1}{2} \ln \frac{2m_e c^2 \beta^2 \gamma^2 W_{max}}{I^2} - \beta^2 - \frac{\delta(\beta\gamma)}{2} \right] \qquad (2.3)$$

where z is the charge of the incident particle and m_e the electron mass. W is the energy transferred to an electron in a single collision, I is the mean excitation energy and $\delta(\beta\gamma)$ is a correction factor. The Bethe equation can be parametrised by [19]

$$f(\beta\gamma) = \frac{P_1}{\beta^{P_4}} \left[P_2 - \beta^{P_4} - \ln \left(P_3 + \frac{1}{(\beta\gamma)^{P_5}} \right) \right] \qquad (2.4)$$

where P_{1-5} are fit parameters.

Fig. 2.4 makes clear how the charged particle identification is provided by the measurement of the energy loss dE/dx, which is proportional to the induced signal at the endplates, together with the particle momentum. The selection of particles of a certain species in the analysis can be reached by using the deviation n of the measured energy loss from the expected mean energy loss under the mass hypothesis of the particle, in terms of the resolution σ of the measurement, (eq. 2.5) as a selection criterion:

$$n = \frac{\frac{dE}{dx}_{measured} - \left\langle \frac{dE}{dx} \right\rangle}{\sigma}. \qquad (2.5)$$
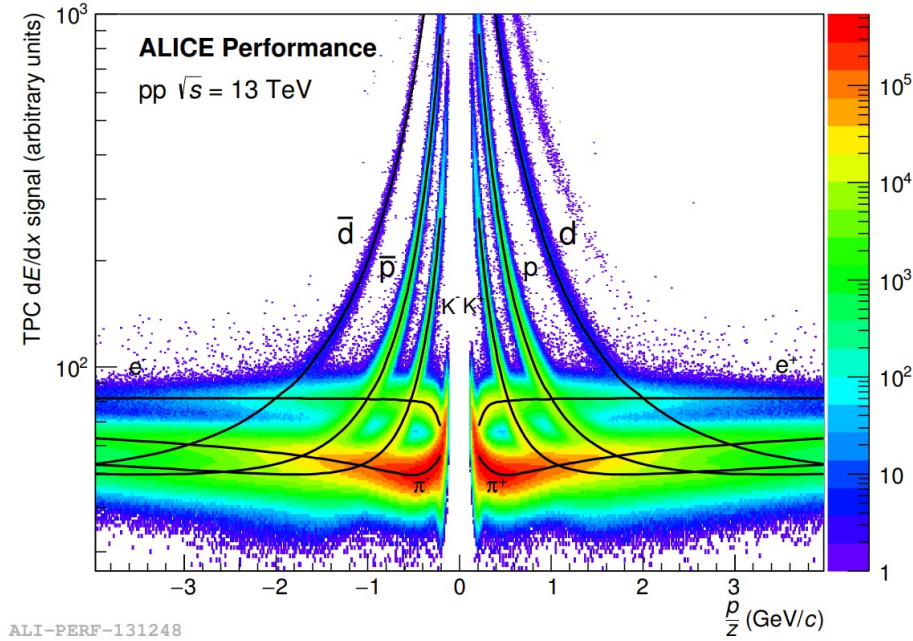
Figure 2.4: Measured, specific energy loss in the TPC depending on the rigidity (momentum divided by charge) of the corresponding particles. The black lines represent the expected energy loss, calculated with the mass hypothesis of the indicated particle.

2.2 Event Reconstruction

A so called *event* in the detector consists of a collision described by a main interaction point referred to as primary vertex (PV) and a variety of tracks emerging from this collision, which are measured in the detector. The question arises how the huge number of particles emerging from the central collisions of the two hadron beams and leaving hits in the form of binary data in the different detector parts can actually be turned into meaningful physical objects that can be identified and fully characterised. This happens during the event reconstruction where the tracking in the central barrel plays a major role.

In the previous section we used the TPC detector as an example to explain the effect of charged particles travelling through the detector material. Each particle carrying an electric charge induces discrete signals measuring the position in space where it has passed a certain point of the detector. The resulting task is to allocate these space points to individual tracks and reconstruct the related kinematics. Due to the high charged-particle multiplicity density, the track finding and particle identification becomes a challenging task [19].

15

2.2.1 Central Barrel Tracking

As mentioned before, the main tracking capability of ALICE lies with the central barrel detectors and in particular with the TPC. The tracking process [19] involves several reconstruction steps.

The first step towards the reconstruction of a track is the clusterisation process which is performed separately for each detector. During this process the detector signal is converted into clusters characterised by their position and the related errors and interpreted as the crossing point of the belonging track.

The tracking in the central barrel then starts with the estimation of a preliminary interaction vertex using clusters in the two layers of the SPD. Pairs of clusters in the SPD are called *tracklets* and the interaction vertex is defined as the point where most of the tracklets converge.

The actual track reconstruction follows an inward-outward-inward scheme [19] starting with the track finding step in the outermost pad-rows of the TPC by building track seeds with several clusters and the position of the estimated interaction vertex as a constraint. Particle tracks not originating from the PV are reconstructed by building track seeds with clusters in the outer regions of the TPC without a contraint to the determined interaction vertex. The built seeds are propagated inwards to the inner TPC radius and updated at each step by assigning clusters that fulfill certain proximity cuts using the *Kalman Filter algorithm*. Only those tracks with at least 20 out of 159 possible clusters in the TPC are accepted for reconstruction. For the propagated tracks a preliminary PID based on the ionisation loss in the TPC is determined.

The reconstructed TPC tracks arising from the described track finding step in the TPC are then propagated to the outer layer of the SSD. They become the seeds for track finding in the ITS which follows in principle the scheme used for the TPC but with respect to the higher track density. For each TPC track a decision tree is built and filled with all prolongation candidates fitted to exactly this track sorted by their reduced χ^2. After applying an algorithm preventing two tracks from sharing several clusters between each other, the track with the highest quality according to its χ^2 from each decision tree is added to the reconstructed event. With those clusters not used for the TPC-ITS tracks, a standalone ITS reconstruction is done due to the decreasing acceptance and reconstruction efficiency for low momenta in the TPC.

In the second step the reconstructed tracks are first extrapolated to their point of clos-

est approach to the preliminary interaction vertex and then propagated in the outwards direction by the use of the Kalman Filter algorithm and of the clusters found in the track finding stage. At each fitting step several informations are updated until the fitting reaches the TRD where the tracks are matched to tracklets in the six layers of the subdetector. In a similar way the tracks are matched afterwards to clusters in the TOF and signals in the EMCal, PHOS, and HMPID.

In the last step the reconstructed tracks are again propagated from the outer TPC radius inwards to the interaction vertex and the track state vector parameters together with its covariance matrix are determined. The last stage of the tracking procedure is the final determination of the interaction vertex by a precise vertex fit using weighted tracks to suppress the contribution of outliers.

2.3 Event Generator and Detector Simulation

In this analysis, data generated in Monte Carlo (MC) simulations is analysed in order to test and compare it to real data originating from pp collisions. MC simulations are based on a great number of random experiments and they are used in particle physics to simulate events of particle collisions. The event generator that is used in this analysis is the PYTHIA6 [20] program for particle simulation at high energy scales. With the input of elementary processes and for example branching fractions of particle decays, primary collisions are simulated including the full information of all emerging particles (e.g. PID information, momentum) [15]. The simulated final-state particles are transported through the detector material by the detector response simulation code GEANT3 [21]. In this way, the detector interaction as well as the energy deposition in the material that generates the detector response are simulated. In the next step the clusters are digitised and the result resembles closely the real data produced by the detector. This raw data are reconstructed and analysed in the same way as the real data.

As a consequence, the simulated data can be used for comparison with the real data. Above all, it is possible to look at the characteristics of different particle types and species which are not distinguishable in real data.

3 Analysis Strategy

3.1 Analysis Motivation

The study of charmed baryon production in pp collisions is a crucial step on the way to understanding charm hadronisation processes in the presence of a QGP state. In order to contribute to this investigation, the full reconstruction of the Ξ_c^0 baryon via its hadronic decay channel in pp collisions at $\sqrt{s} = 5.02\,\text{TeV}$ has been carried out for the first time in ALICE. This reconstruction serves as the underlying analysis of the work that is done in this thesis and contributes to the test of the universality of the charm fragmentation function.

The complex decay topology is reconstructed using the KF Particle package for the reconstruction of full short-lived particle decay topologies. The features that are provided by the KF package are of vital importance for the search for rare signals like the Ξ_c^0. The aim of this analysis is to validate and test the possibility to implement the software package within the ALICE software framework. Therefore, different selection criteria for the secondary decay vertex reconstruction of Λ and Ξ particles in the Ξ_c^0 decay, provided by KF Particle, are investigated and tested.

3.2 Full Reconstruction of the Ξ_c^0 Hadronic Decay

In pp collisions a variety of different particle species are produced. In gerneral they can be divided into *long-lived* and *short-lived* particles [22]. Long-lived particles are either stable particles, such as protons or electrons, or particles with a decay length large enough to cross the tracking system of the detector. These particles, provided they are charged, interact with the detector material and their track can be fully reconstructed. Short-lived particles, on the other hand, do not decay within the acceptance of the tracking system due to their small life time. Therefore, they can only be measured indirectly by reconstructing their decay particles. However, the measurement of short-lived particle species, including charmed mesons and baryons, provides insight into important physical phenomena. Therefore, it is crucial to be able to reconstruct decay chains originating from short-lived particle decays.

Fig. 3.1 schematically shows the weak decay of the Ξ_c^0 baryon. The short-lived Ξ_c^0 baryon is produced in the collision with its production vertex denoted as primary vertex (PV).
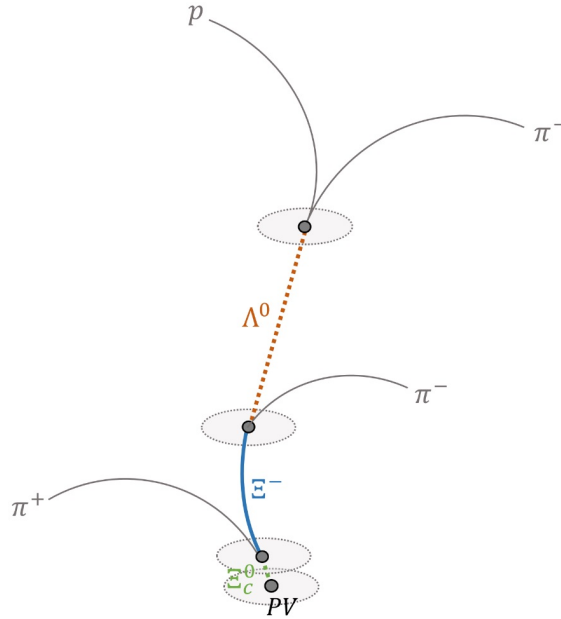
Figure 3.1: Sketch of the baryonic decay of the Ξ_c^0 baryon (no realistic scale). The primary vertex (PV) is the main interaction point of the underlying event where the Ξ_c^0 baryon is produced. The localisation errors of the vertices are indicated in gray.

It decays into a pion (π) and a charged Ξ baryon which further decays into a Λ baryon and another π. The neutral Λ baryon cannot be detected and it is reconstructed from its decay particles: unlike sign tracks of a proton (p) and a π. This type of decay of neutral mother particles into a pair of daughter particles with opposite charge is referred to as V^0 decay. The properties of the particles created in the decay cascade of the Ξ_c^0 baryon are listed in Tab. 3.1.

The so called *secondary vertices* are the decay vertices of short-lived particles. Therefore, they are also the production points of their decay products which are called *secondary*

Table 3.1: Cascade Particles [2].

Particle	Quark Content	Mass (MeV/c^2)	Mean Lifetime (s)	Decay Length cτ (m)
Ξ_c^0	dsc	2470.88	$112 \cdot 10^{-15}$	$33.6 \cdot 10^{-6}$
Ξ^-	dss	1321.71	$1.639 \cdot 10^{-10}$	$4.9 \cdot 10^{-2}$
π^+	u$\bar{\text{d}}$	139.57018	$2.6033 \cdot 10^{-8}$	7.8
Λ^0	uds	1115.683	$2.632 \cdot 10^{-10}$	$7.9 \cdot 10^{-2}$
p	uud	938.272046		stable
π^-	$\bar{\text{u}}$d	139.57018	$2.6033 \cdot 10^{-8}$	7.8

tracks. Most of the secondary tracks do not overlap with the errors of the PV. In contrast, *primary tracks* represent particles that are produced within the errors of the PV.

The usual method of reconstructing short-lived particles is the direct calculation of the mother particle's parameters by summing up the parameters of its daughters at their production point. In the case of the V^0 decay of Λ the daughter tracks are fully reconstructed as infinite helices in space. The secondary vertex is reconstructed by calculating the point of the distance of closest approach (DCA) between the two tracks. Subsequently their parameters are extrapolated to this point [22]. In this way the mother particle is reconstructed at its decay point.

In contrast to the usual approach, in this thesis the reconstruction of the Ξ_c^0 decay chain is perfomed by the use of the *KF Particle package.* This software is based on the Kalman filter method and has been developed for the complete reconstruction of short-lived particles.

3.3 Kalman Filter Method

The Kalman filter algorithm [23] takes a set of k random variables (measurements) and provides an optimal estimate for an unknown state vector $\mathbf{r}$ with its covariance matrix $\mathbf{C}$. The covariance matrix contains all covariances of the state vector with the variances of the single state vector components on its diagonal. The algorithm starts with an initial approxiamtion of $\mathbf{r}$ and $\mathbf{C}$. With the knowledge of the impact of one measurement on the change of the state vector, a prediction of the evolution of $\mathbf{r}$ and of the covariance matrix is made, based on this first approximation. In the next step the first measurement is taken into account and an optimum estimation of the vector according to this measurement is calculated via a geometric fit. This filtration step is repeated for every k^{th} measurement, refitting with all previous $(\mathrm{k}-1)$ measurements. The estimate obtained after the filtration of the last measurement is the optimal estimation of the state vector with its covariance matrix.

3.4 KF Particle Package

The KF Particle package allows a full reconstruction of a decayed particle with its decay vertex, its momentum, and energy together with the covariance matrix. In contrast to other vertexing packages, KF Particle provides a direct estimation of the particle's pa-

rameters and of the associated covariance matrix in addition to the reconstruction of the production and decay vertices [24].

The first step in the reconstruction of the decayed mother particle is the initial approximation of the position of the decay point and the particle momentum and energy. This determination is based on the estimates of the daughter tracks. The Kalman filter algorithm used in the KF software takes a natural parametrisation of the particle as the state vector [24]:

$$\mathbf{r} = (x, y, z, p_x, p_y, p_z, E)^T. \tag{3.1}$$

After the first approximation of the decay vertex one of the daughter particles is transported to this initial vertex approximation. The next step is the calculation of the daughter particle's approximated momentum and its covariance matrix at the initial vertex position. The estimate of the daughter is then used for the filtration step of the Kalman filter in order to provide the estimation of the mother particle's state vector and covariance matrix. This procedure is repeated for the next daughter track until all daughters of the decayed particle are treated. After the reconstruction of the decayed particle at the decay vertex, the parameter $s = \frac{l}{p}$ is added to the state vector $\mathbf{r} = (x, y, z, p_x, p_y, p_z, E, s)^T$, where l is the length of the particle trajectory in the laboratory coordinate system and p the momentum [24]. In the last, optional step all parameters of the particle are transported to the production vertex which is used as a measurement for the filtering of the particle's parameters at this production vertex.

The final optimal estimation of the state vector and its covariance matrix contains all information needed to obtain a full description of the particle, both at the production and at the decay vertex [24]. Hence, KF Particle allows the determination of the particle track in its full extent. Some information, that is not explicitly included in the state vector, can be easily calculated. The particle momentum p, the invariant mass M, the length of flight in the laboratory system, and the life time cτ are determined as follows [24]:

$$
\begin{aligned}
p &= \sqrt{p_x^2 + p_y^2 + p_z^2} \\
M &= \sqrt{E^2 - (p_x^2 + p_y^2 + p_z^2)} \\
L &= sP \\
c\tau &= sM.
\end{aligned}
\tag{3.2}
$$

After assigning certain daughter tracks to a reconstructed secondary vertex, they can be removed from the PV fit. In the same way the reconstructed decay particles can be added to the PV fit if it corresponds to their production vertex and the vertex precision can therefore be improved.

In contrast to other reconstruction methods, KF Particle allows to actually move tracks within their uncertainties to make them fit to a certain vertex. This results in an improved estimation of the particles' parameters.

3.4.1 KF Constrained Fits and Variables

During the reconstruction of decays it is possible to improve the estimate of the state vectors by applying certain constraints on the state vector parameters. These constraints are treated as regular measurements by the Kalman filter. Thus, they are taken into account as additional information in the fitting procedure.

In the case of the reconstruction of secondary vertices, an assumption can be made regarding the mass of the mother particle. In order to take this assumption into account, a constraint is applied to the state vector parameters during the fitting of the mother particle in the way that the particle is required to have a certain invariant mass. This is called the *mass constraint*.

In the case that an assumption can be made on a particle's production vertex, a *topological constraint* can be set to the state vector parameters. Here, the *topological constraint* requires the particle to point to its production vertex. The topological constraint can also be used to force a particle to point to any reconstructed vertex.

KF uses different variables to describe decay topologies that can be used as criteria for the selection of certain reconstructed candidates.

$\chi^2_{\text{geo}}/\text{NDF}$ Variable

The $\chi^2_{\text{geo}}/\text{NDF}$ refers to the geometrical fitting procedure for the reconstruction of a decayed particle by its daughter particles. It expresses the quality of the fit: small values of χ^2 correspond to a good fit quality, whereas large values stand for a bad quality of the fit. NDF is the number of degrees of freedom, corresponding to the number of measurements that are taken into account in the fitting routine. Consequently, $\chi^2_{\text{geo}}/\text{NDF}$ describes whether the trajectories of the daughter tracks of a decay intersect within their uncertainties [22]. The smaller the obtained value, the larger is the probability that the tracks intersect within their errors. Therefore, it characterises the quality of the reconstruction of the mother particle. Nevertheless, if the uncertainties on the tracks are

extremely large the value of χ^2 will also indicate a good fit quality.

χ^2_{topo}/NDF Variable

In the case of a reconstructed candidate that has been assigned to a production vertex using a topological constraint, the χ^2_{topo}/NDF reflects the probability that the particle truely emerges from that vertex. It characterises whether a particle is produced in the region of the production vertex taking into account the localisation error of the vertex [22]. Again, the probability of the particle to point back to the vertex is high if the χ^2_{topo}/NDF value of the corresponding fit is small.

l/Δl Variable

Another variable provided by the KF package is the distance between the PV of the event and the decay point of a reconstructed candidate, normalised by its error l/Δl. This variable describes how far away from the PV the candidate has decayed, in terms of the localisation errors of the vertices [22].

3.5 Reconstruction Procedure

The minimum bias triggered data sample used for the full reconstruction of Ξ^0_c originates from pp collisions at a centre-of-mass energy of $\sqrt{s} = 5.02\,\text{TeV}$ recorded by ALICE in the year 2017. In total, about 900 million events are analysed. The corresponding, simulated MC data contain about 30 million events.

3.5.1 Event Selection

Not all of the events that are measured by the detector can be used in the analysis. Before the Ξ^0_c is actually reconstructed, different selection criteria are required to be satisfied by the events in the offline analysis of the data, in order to select those events that are relevant for the reconstruction. So called *Pile-up events* can occur, where more than one collision takes place. Therefore, more than one PV is reconstructed and tracks from different collisions are measured in the detector. These events are rejected for real data in the offline event selection. Furthermore, only events with a PV that is reconstructed within the range of $\pm10\,\text{cm}$ from the centre of the detector coordinate system along

the z-direction are taken into account in the analysis. This range corresponds to the acceptance of the detector.

3.5.2 Reconstruction Strategy and Track Selection

The reconstruction of Ξ_c^0 begins with the reconstruction of the V^0 decay by selecting unlike sign tracks of protons and pions. This is done by reconstructing the secondary decay vertex after the full reconstruction of the single daughter tracks, which is referred to as offline V^0 reconstruction.

The PID of the two daughter tracks is ensured by the dE/dx measurement in the TPC. Protons and pions are selected with the criteria $|n\sigma_{\text{TPC}}|(p) < 4$ and $|n\sigma_{\text{TPC}}|(\pi) < 4$. Especially for higher p_{T}-ranges, where the TPC is not able to separate different particle species, the distinction between protons and pions is rather difficult. The V^0 decay of $K_s^0 \rightarrow \pi^+\pi^-$ has a rather similar decay topology to the Λ decay. Therefore, the selected V^0 candidates are required to have an invariant mass that is incompatible with the mass of a K_s^0 meson that is calculated by two pion tracks. This means that candidates with a mass in the range of $10\,\text{MeV}/c^2$ of the mass of K_s^0 are rejected. This selection is called competing V^0 rejection.

Furthermore, the two daughter tracks have to meet several requirements regarding the detector response: the number of the clusters that are induced by the particles in the TPC, as well as the number of crossed rows should be larger than 70, whereas the number of clusters used for the determination of the specific energy loss must be at least 50. The ratio of the number of crossed rows and the number of findable clusters in the TPC is required to be larger than 0.8. Finally, for the pseudorapidity of the daughter particles the criterion $|\eta| < 0.8$ must apply.

The next step is the reconstruction of the Ξ decay vertex by combining the selected Λ candidates with tracks of secondary pions. For these pion tracks the same track selection criteria as for the V^0 daughter particles are applied. Additionally, the pion is required to have a transverse momentum that is larger than $0.15\,\text{GeV}/c$ which is the minimum transverse momentum of particles that are only reconstructed with the TPC.

In the last step of the reconstruction, the Ξ candidates are combined with another pion track that fulfils the same selection criteria as before, apart from its transverse momentum which is required to be above $0.5\,\text{GeV}/c$. Furthermore, the pion track must leave more than 3 hits in the ITS to ensure that the particle is produced in the area of the PV. Due to the limited detector resolution, the reconstructed decay vertex of the Ξ_c^0 cannot be separated from the PV.

4 Analysis and Results

Λ and Ξ candidates, that are either primary particles produced at the PV or secondary decay particles are reconstructed from the MC data sample. In Tab. 4.1 the number of reconstructed candidates of the different particles are shown respectively. In the real data sample it is not possible to distinguish between these different types of candidates.

Table 4.1: Reconstructed particles from the MC data sample.

particle	number of primary candidates	number of secondary decay candidates
Λ^0	420 000	120 000
$\bar{\Lambda}^0$	390 000	100 000
Ξ^-	17 000	50
Ξ^+	15 500	40

4.1 Invariant Mass

The mass of the reconstructed particles is determined by calculating the invariant mass M of the two daughter particles which is equal to the mass of the particle in the rest frame. The four-vectors of the two decay particles' momentum

$$p_i^\mu = \left(\frac{E_i}{c}, \mathbf{p}_i \right), \quad i = 1, 2 \tag{4.1}$$

are given by their energy E and their momentum vector $\mathbf{p}$. The squared invariant mass is calculated as the square of the sum of the two four-vectors:

$$M^2 = (E_1 + E_2)^2 - \|\mathbf{p}_1 + \mathbf{p}_2\|^2. \tag{4.2}$$

In Fig. 4.1a and 4.1b the Λ and $\bar{\Lambda}$ invariant masses are shown respectively. The primary candidates, which are indicated by the red markers, are either produced in the initial fragmentation process or in short-lived particle decays such as the Σ^0. The fraction of these particles is high compared to the number of secondary decay particles, which are represented by the green histogram. The contributions from daughter tracks that have

(a) Λ invariant mass.

(b) $\overline{\Lambda}$ invariant mass.

(c) Ξ^- invariant mass.
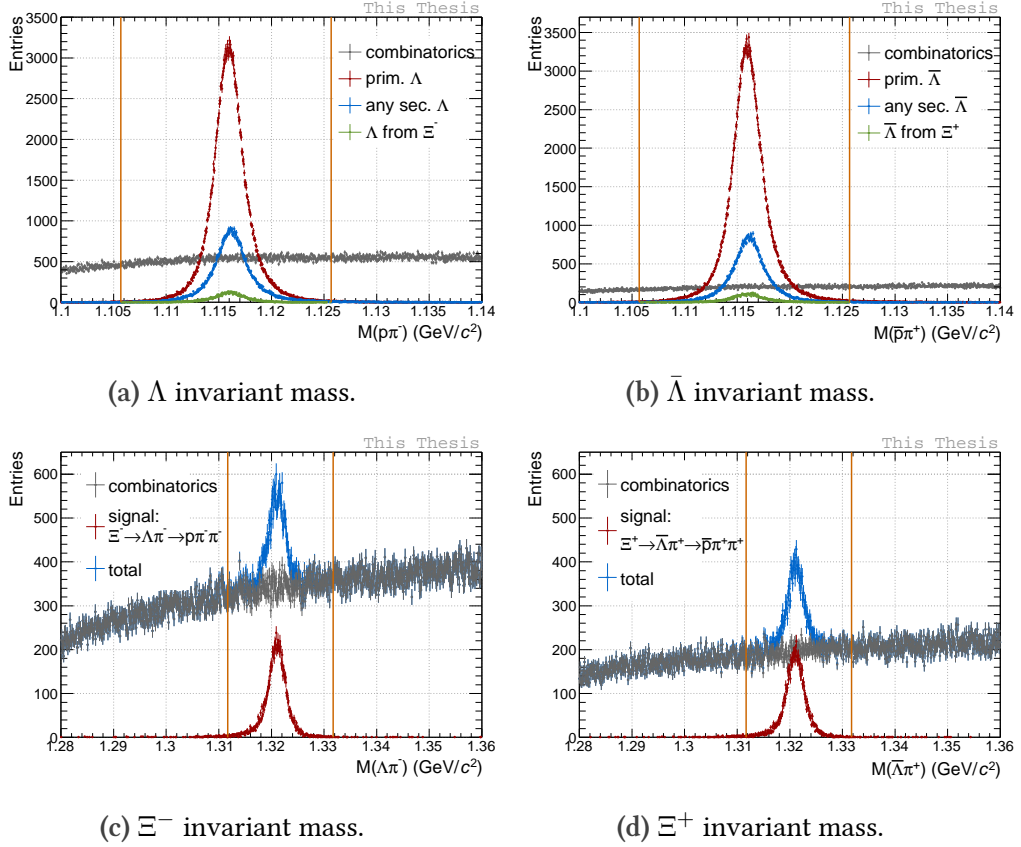
(d) Ξ^+ invariant mass.

Figure 4.1: Invariant masses of the reconstructed V^0 and cascade candidates calculated by their daughter particles. The solid lines indicate the mass range which is selected for the analysis.

been paired wrongly form the combinatorial background distribution which is shown by the gray markers. The $\overline{\Lambda}$ is reconstructed from a positively charged π and an antiproton ($\overline{p}$). The $\overline{p}$ annihilate with the p of the detector material. Consequently, the combinatorial background from the $\overline{\Lambda}$ is smaller with respect to the reconstructed Λ due to fewer particles and, therefore, fewer possibilities of daughter track combinations.

The invariant masses of the Ξ^- and Ξ^+ candidates in Fig. 4.1c and 4.1d show a similar behaviour of the background distribution as a consequence of the lower background for the $\overline{\Lambda}$ candidates. Due to the limited detector resolution in ALICE, the Ξ candidates are defined as primary particles although they can be physically secondary particles.
In order to reject the largest part of the combinatorial background on both sides of the mass peak, the invariant mass of the candidates is required to lie within a certain range of the referred PDG-mass [2] (listed in Tab. 3.1). The limit on the candidates' mass is in-

dicated in Fig. 4.1 by the solid, vertical lines. Thus, candidates in MC and in real data are selected according to the following selection criteria: $\|m(\Lambda) - m(\Lambda)_{\mathrm{PDG}}\| < 0.01\,\mathrm{GeV}/c^2$ and $\|m(\Xi) - m(\Xi)_{\mathrm{PDG}}\| < 0.01\,\mathrm{GeV}/c^2$. Consequently, all candidates below the invariant mass peak, including both signal and background, are selected due to the fact that they cannot be distinguished in real data.

Furthermore, only candidates at midrapidity, corresponding to the detector acceptance, are used in the analysis: $\|y(\Lambda)\| < 0.5$ and $\|y(\Xi)\| < 0.5$.

4.2 Topological Studies

In the first part of the analysis the geometric variables $\chi^2_{\mathrm{geo}}/\mathrm{NDF}$ and $l/\Delta l$ provided by KF, which can be potentially used as selection criteria, are investigated.

The p_{T}-differential production cross section of the Ξ^0_c baryon is determined from the reconstructed candidates in the real data sample. During the reconstruction procedure, candidates that do not fulfil the applied selection criteria are rejected and not taken into account. Hence, the reconstruction has a certain efficiency that can only be computed from MC data. Therefore, the distributions of the variables in real data and MC must be compared and found to be consistent in order to validate the possibility of using them to improve the particle selection and to ensure a proper efficiency correction.

The discrepancy between the real data and MC distributions for the $\chi^2_{\mathrm{geo}}/\mathrm{NDF}$ variable is larger for the Λ candidates in Fig. 4.2a than for the $\bar{\Lambda}$ candidates (Fig. 4.2b). This means that the mismatch between real and simulated data, that can be observed in Fig. 4.2a, corresponds to the difference in the background distributions below the invariant mass peak. The analogue investigation of the Ξ candidates (Figs. 4.2c and 4.2d) leads to the same result.

In the following, the results of the study are outlined only for the reconstructed $\bar{\Lambda}$ and Ξ^+ candidates because of the smaller background in these two cases compared to their reconstructed charge conjugates. In the case of the $l/\Delta l$ variable, Fig. 4.3 shows a clear consistency between real data and MC, both for $\bar{\Lambda}$ and Ξ^+ candidates. These results justify the possible application of $\chi^2_{\mathrm{geo}}/\mathrm{NDF}$ and $l/\Delta l$ as selection criteria for all Λ and Ξ particles.

In the next step the MC distributions of the KF variables for the different candidates have been investigated in order to test their behaviour.
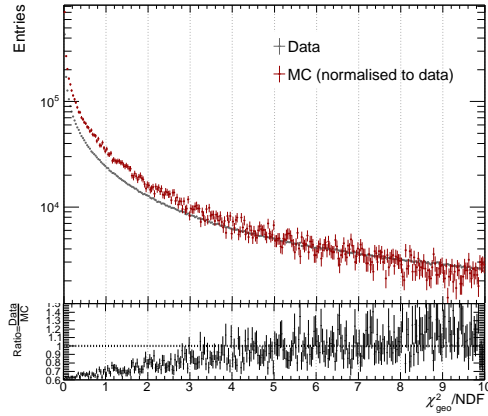
The distributions of the $\chi^2_{\mathrm{geo}}/\mathrm{NDF}$ variable for signal and background in MC are shown in Fig. 4.4a and 4.4b respectively. The aim of $\chi^2_{\mathrm{geo}}/\mathrm{NDF}$ as a selection criterion is the
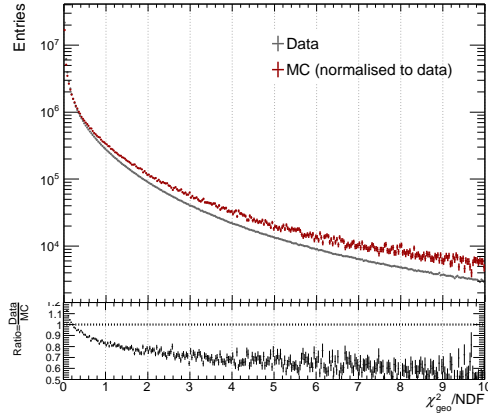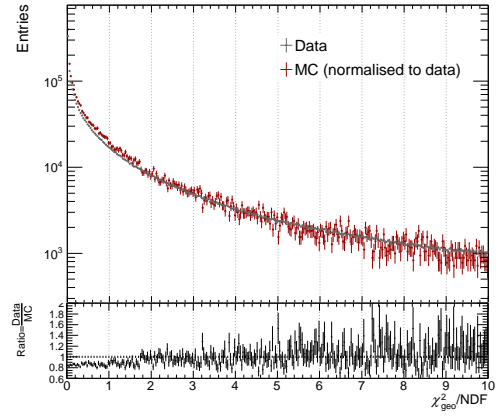
(a) Λ candidates.
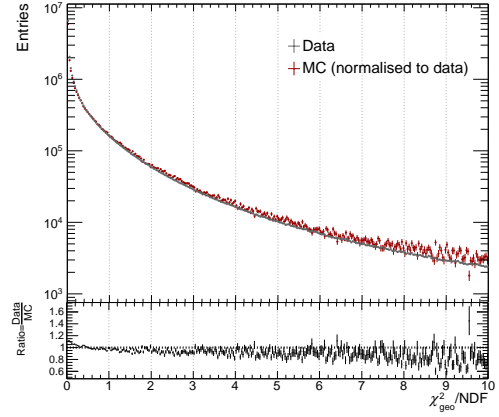
(b) $\bar{\Lambda}$ candidates.

(c) Ξ^- candidates.

(d) Ξ^+ candidates.

Figure 4.2: Distributions of the $\chi^2_{\text{geo}}/\text{NDF}$ variable for the different reconstructed candidates in real data and in MC normalised to real data.
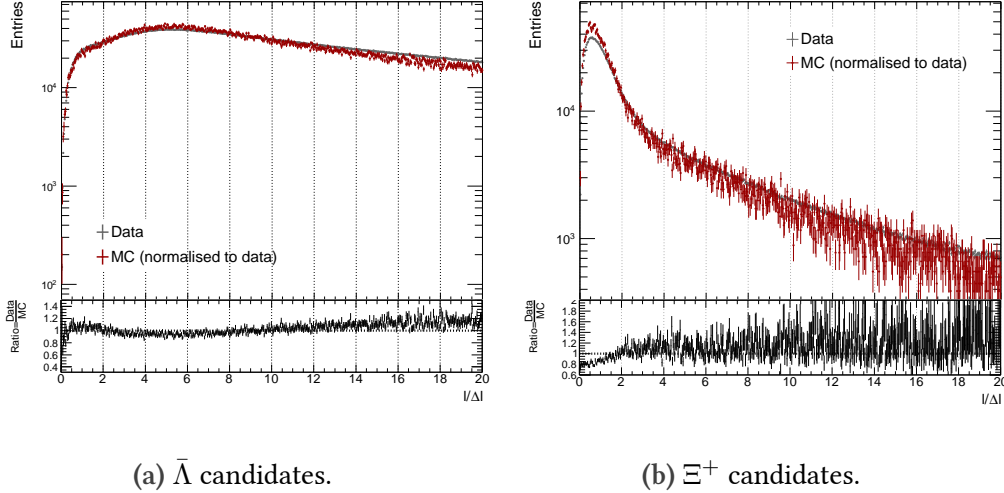
(a) $\bar{\Lambda}$ candidates.

(b) Ξ^+ candidates.

Figure 4.3: Distributions of the $l/\Delta l$ variable for the different reconstructed candidates in real data and in MC normalised to real data.

rejection of background together with the possibility to preserve the majority of the signal candidates, which is an important aspect in the search for the rare signal of Ξ_c^0. The distribution in Fig. 4.4a verifies the usability of $\chi^2_{\mathrm{geo}}/\mathrm{NDF}$ for the selection of $\bar{\Lambda}$ particles. Signal candidates usually have small $\chi^2_{\mathrm{geo}}/\mathrm{NDF}$ values. Consequently, the signal distribution is peaked stronger at small $\chi^2_{\mathrm{geo}}/\mathrm{NDF}$ values and has a steeper rise than the combinatorial background distribution. The difference between the two distributions allows to reject background and to preserve the signal candidates emerging from a real $\bar{\Lambda}$ decay. A possible selection on the variable could be $\chi^2_{\mathrm{geo}}/\mathrm{NDF}(\bar{\Lambda}) < 2$ and $\chi^2_{\mathrm{geo}}/\mathrm{NDF}(\Lambda) < 2$ which is applied in the selection for the presented analysis.

The distinction between Ξ^+ signal and background is not necessarily guaranteed by a selection of certain values of $\chi^2_{\mathrm{geo}}/\mathrm{NDF}$ due to the similarity between the $\chi^2_{\mathrm{geo}}/\mathrm{NDF}$ distributions of signal and background candidates, which is shown in Fig. 4.4b. One possibility to use this variable as a selection criterion would be a constraint which rejects all candidates that have a larger $\chi^2_{\mathrm{geo}}/\mathrm{NDF}$ value than the majority of the Ξ^+ signal. This ensures to reject as many background candidates as possible. The criteria used in this analysis for the selection of Ξ particles are the following: $\chi^2_{\mathrm{geo}}/\mathrm{NDF}(\Xi^+) < 3$ and $\chi^2_{\mathrm{geo}}/\mathrm{NDF}(\Xi^-) < 3$.

The same investigations have been done on the $l/\Delta l$ variable for the reconstructed $\bar{\Lambda}$ and Ξ^+ candidates (see Fig. 4.5). Fig. 4.5a reveals a clear difference between the background and signal distributions. The large decay length of Λ baryons leads to the fact
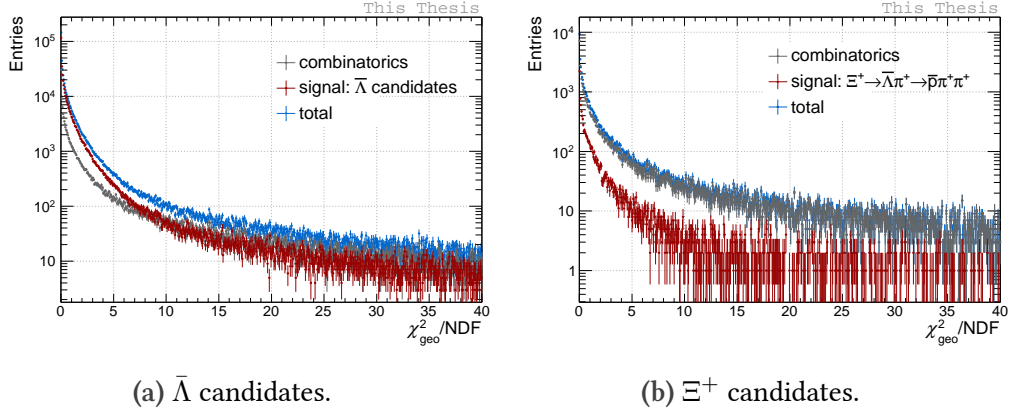
(a) $\bar{\Lambda}$ candidates.

(b) Ξ^+ candidates.

Figure 4.4: Background and signal distributions of the $\chi^2_{\mathrm{geo}}/\mathrm{NDF}$ variable for the different reconstructed candidates in MC.

(a) $\bar{\Lambda}$ candidates.
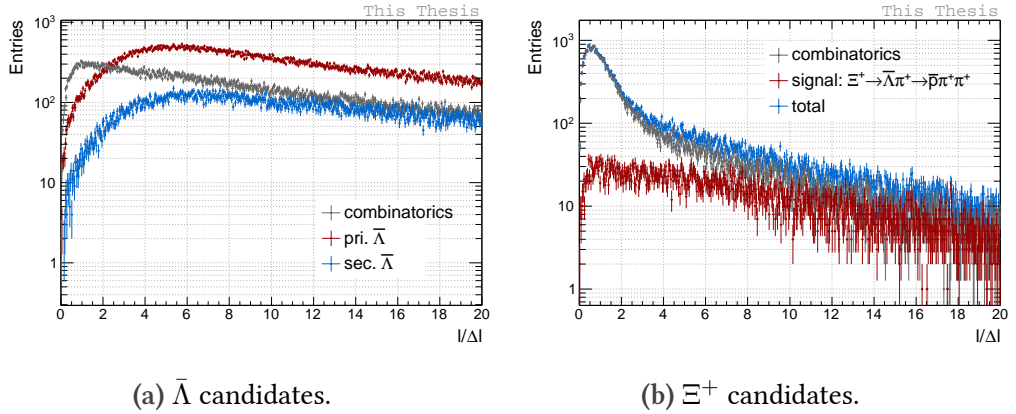
(b) Ξ^+ candidates.

Figure 4.5: Background and signal distributions of the $l/\Delta l$ variable for the different reconstructed candidates in MC.

that the $l/\Delta l$ distribution for primary particles rises rather slowly. The distribution for the secondary candidates shows an even less steep rise due to the additional contribution to the distance to the PV by the decay length of their mother particle. However, the combinatorial background is distributed more uniformly but also rises for small values of $l/\Delta l$ due to the fact that the track density is higher for small distances to the PV. A selection using this variable allows to remove a large part of the background and to select secondary particles rather than primaries. This is why $l/\Delta l(\bar{\Lambda}) > 3$ and $l/\Delta l(\Lambda) > 3$ are applied in this analysis as a possible criterion in the selection of secondary $\bar{\Lambda}$ and Λ candidates.

Fig. 4.5b shows the corresponding distributions for the reconstructed Ξ^+ candidates. The smaller decay length of Ξ baryons compared to Λ particles is reflected in the dis-

tribution of the Ξ^+ signal candidates. The combinatorial background is peaked at small values of $l/\Delta l$. This could possibly be reflecting the fact that most of the Λ baryons, which are used for the reconstruction of Ξ and, therefore, are included in the combinatorial background, are primary particles.

In this analysis the following selection criterion is applied to the reconstructed Ξ candidates: $l/\Delta l(\Xi^+) > 2$ and $l/\Delta l(\Xi^-) > 2$.

4.2.1 Systematic Study of Efficiency, S/B Ratio and Significance

The χ^2_{geo} and $l/\Delta l$ variables are now tested according to their performance in cleaning the data sample from background and preserve as much signal as possible. There are three quantities which provide information about the composition of a data sample and the quality of the reconstruction procedure, at least to a certain extent: the reconstruction efficiency, the significance, and the signal-to-background ratio.

The reconstruction *efficiency*, ϵ_{MC}, describes how many particles are reconstructed, N_{rec}, compared to the number of particles that have been generated, N_{gen}, in the MC simulation. The reconstruction efficiency is defined as

$$\epsilon_{MC} = \frac{N_{rec}}{N_{gen}}. \tag{4.3}$$

It includes the considered detector acceptance as well as the actual reconstruction of the simulated particles. In the case of rare signals, the reconstruction efficiency should be high in order to maximise the total number of signal candidates preserved in the sample. The *significance* of a data sample is defined as

$$S = \frac{S_{rec}}{\sqrt{S_{rec} + B_{rec}}}. \tag{4.4}$$

S_{rec} is the number of reconstructed signal candidates and B_{rec} the number of reconstructed background candidates, which are all satisfying the applied limit on the particle mass (see Sec. 4.1). The significance of the signal is especially important in the case of the reconstruction of rare signals. The *signal-to-background ratio* describes the ratio between the number of reconstructed signal and background candidates, $S_{\text{rec}}/B_{\text{rec}}$. In general the signal-to-background ratio should be kept large during the particle reconstruction and selection.

In Fig. 4.6 the efficiency and the signal-to-background ratio of the reconstructed $\bar{\Lambda}$ can-

didates are shown for several $p_{\mathrm{T}}(\bar{\Lambda})$-intervals, depending on the selection criteria of the $\chi^2_{\mathrm{geo}}/\mathrm{NDF}$ and $\mathrm{l}/\Delta\mathrm{l}$ variables that were applied. The shape of the efficiency distribution is not changing much between the different p_{T}-intervals, whereas the maximum value of the efficiency varies with the change of the p_{T}-range.

In contrast, the signal-to-background distribution is changing in its shape with increasing values of p_{T} but its maximum value stays nearly the same. Consequently, a possible selection criterion on $\mathrm{l}/\Delta\mathrm{l}$ and $\chi^2_{\mathrm{geo}}/\mathrm{NDF}$ would have to be varied with the p_{T}-interval in order to maximise the signal-to-background ratio.

The same investigations have been done done on the significance of the reconstructed sample with similar results as for the efficiency.

The distributions in Fig. 4.6 were used in the analysis to find appropriate combinations of selection criteria on $\chi^2_{\mathrm{geo}}/\mathrm{NDF}$ and $\mathrm{l}/\Delta\mathrm{l}$. Subsequently, the efficiency depending on the p_{T} was investigated for several combinations of constraints on the two variables. The results are shown in Figs. 4.7 and 4.8. The efficiency of the reconstruction without any selection criteria comes to about 60% and decreases with the applied criteria. The change in the efficiency amounts to about 10% for the p_{T}-interval of the maximum value, which lies between 2 and $5\,\mathrm{GeV}/c$, as it is shown in Fig. 4.7.

The corresponding signal-to-background distributions are shown in Fig. 4.9, and the ratios with respect to the case in which no selection on the two variables is applied are shown in Fig. 4.10. The distributions reflect the results of the systematic study in Figs. 4.6d, 4.6e, and 4.6f. For $p_{\mathrm{T}} < 1\,\mathrm{GeV}/c$ the signal-to-background ratio can be increased even with loose selection criteria and it varies widely with a change in the values of the criteria. Especially in the mid-p_{T}-range the variation of the criteria does not result in a large change of the value for the signal-to-background ratio.

The same analysis on the quality of the reconstruction depending on the applied selection criteria on $\chi^2_{\mathrm{geo}}/\mathrm{NDF}$ and $\mathrm{l}/\Delta\mathrm{l}$ is carried out for the Ξ baryons. The results for the efficiency and the signal-to-background ratio in the Ξ^+ reconstruction can be seen in Fig. 4.11. The efficiency distribution in Fig. 4.11a reaches its maximum value of about 30% in the p_{T}-interval of 4 to $7\,\mathrm{GeV}/c$. The applied selection criteria cause a reduction of the efficiency whereby the maximum variation is about 10%.
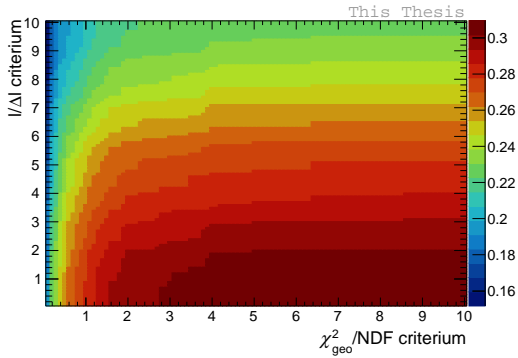
In constrast, the signal-to-background ratio can be improved by the application of criteria on the KF variables $\chi^2_{\mathrm{geo}}/\mathrm{NDF}$ and $\mathrm{l}/\Delta\mathrm{l}$. The change of the criteria's value has a larger impact on the value of the ratio than it is found for the $\bar{\Lambda}$ candidates.
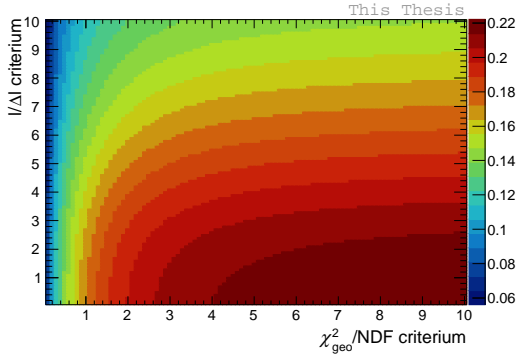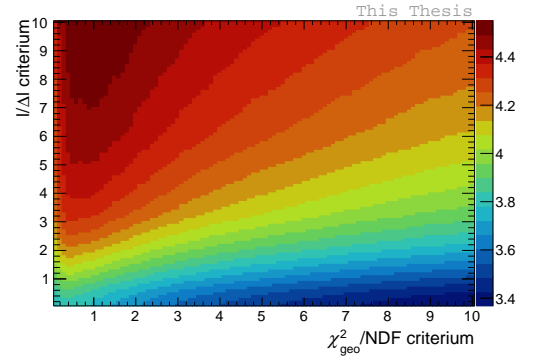
(a) Efficiency of the $\bar{\Lambda}$ reconstruction for candidates with $0 <p_{\mathrm{T}}(\bar{\Lambda})< 4\,\mathrm{GeV}/c$.
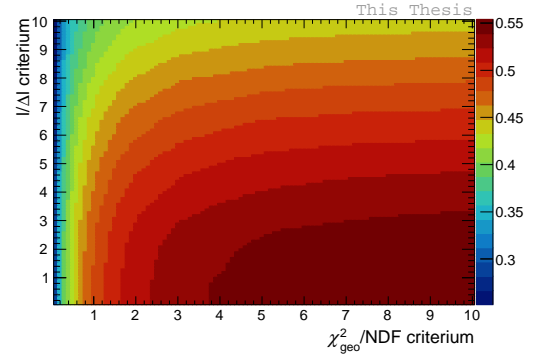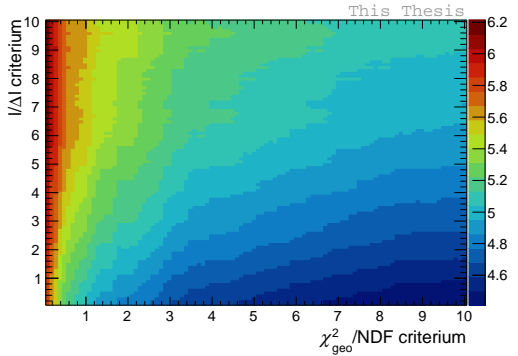
(b) Efficiency of the $\bar{\Lambda}$ reconstruction for candidates with $4 <p_{\mathrm{T}}(\bar{\Lambda})< 8\,\mathrm{GeV}/c$.

(c) Efficiency of the $\bar{\Lambda}$ reconstruction for candidates with $08 p_{\mathrm{T}}(\bar{\Lambda})< 12\,\mathrm{GeV}/c$.

(d) Signal-to-background ratio of the reconstructed $\bar{\Lambda}$ candidates with $0 <p_{\mathrm{T}}(\bar{\Lambda})< 4\,\mathrm{GeV}/c$.

(e) Signal-to-background ratio of the reconstructed $\bar{\Lambda}$ candidates with $4 <p_{\mathrm{T}}(\bar{\Lambda})< 8\,\mathrm{GeV}/c$.
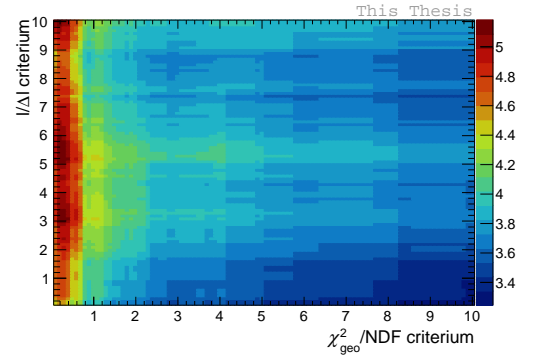
(f) Signal-to-background ratio of the reconstructed $\bar{\Lambda}$ candidates with $8 <p_{\mathrm{T}}(\bar{\Lambda})< 12\,\mathrm{GeV}/c$.

Figure 4.6: Efficiency and signal-to-background ratio for the reconstructed $\bar{\Lambda}$ candidates, depending on the selection criterion of $\chi^2_{\mathrm{geo}}/\mathrm{NDF}$ and $l/\Delta l$, in different p_{T}-intervals.
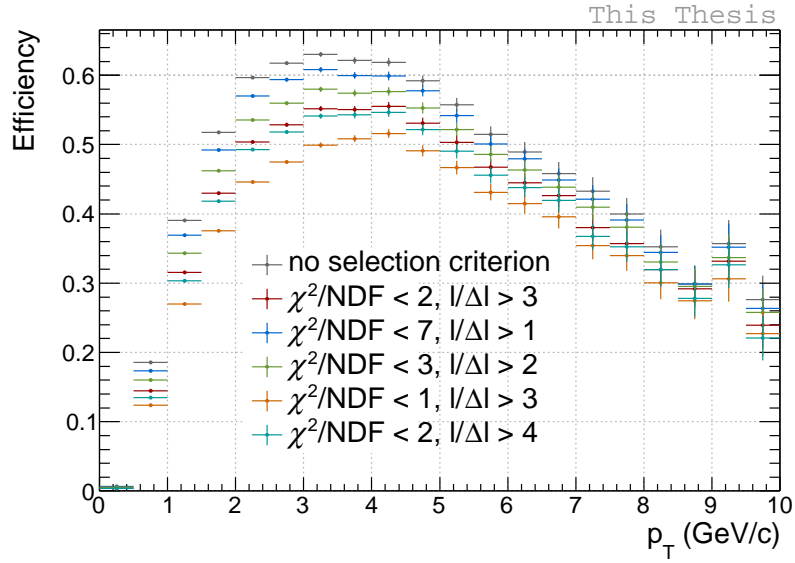
Figure 4.7: Efficiency of the reconstruction of $\bar{\Lambda}$ candidates depending on p_T for different combinations of selection criteria on $\chi^2_\mathrm{geo}/\mathrm{NDF}$ and $l/\Delta l$.
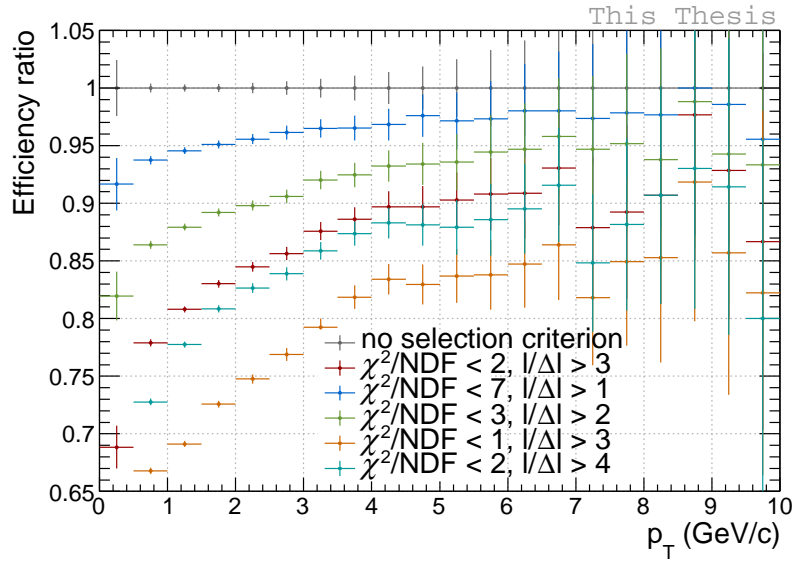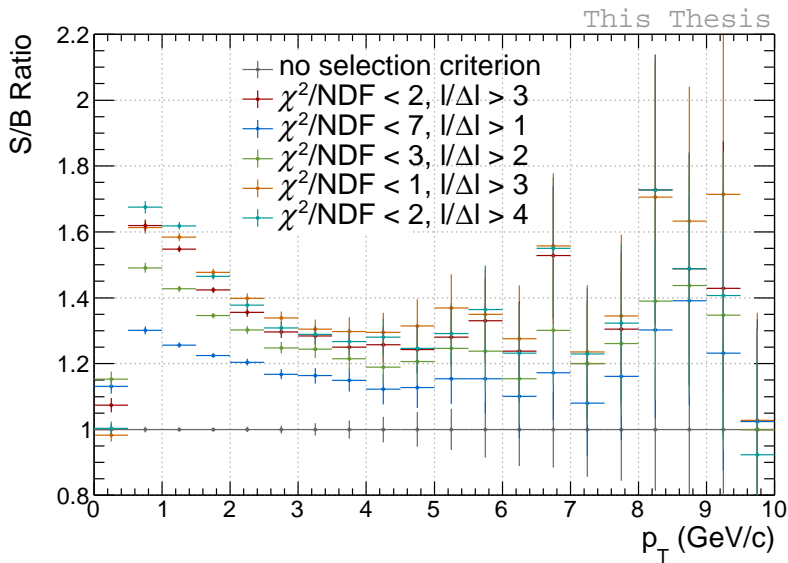

Figure 4.8: Efficiency of the reconstruction of $\bar{\Lambda}$ candidates depending on p_T for different combinations of applied selection criteria on $\chi^2_\mathrm{geo}/\mathrm{NDF}$ and $l/\Delta l$ divided by the reconstruction efficiency without any applied selection criterion.
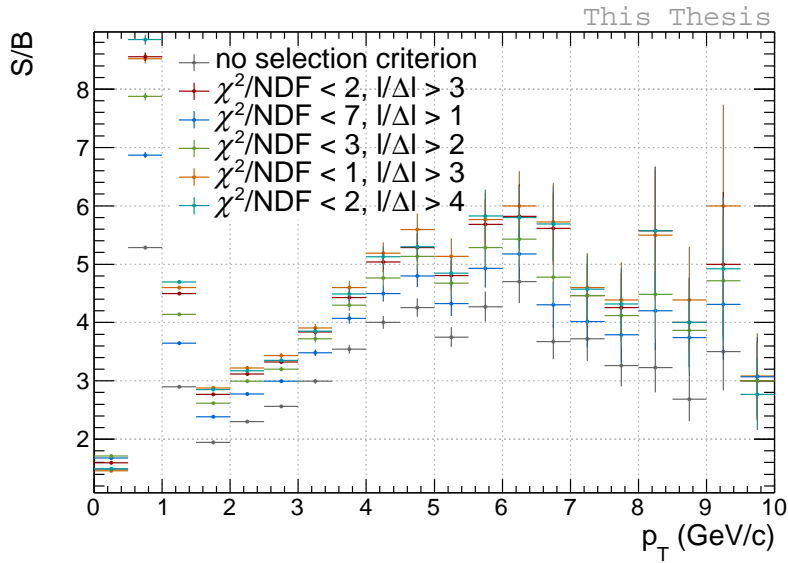
Figure 4.9: Signal-to-background ratio of the reconstructed $\bar{\Lambda}$ candidates depending on p_T for different combinations of selection criteria on $\chi^2_{\mathrm{geo}}/\mathrm{NDF}$ and $l/\Delta l$.

Figure 4.10: Signal-to-background ratio of the reconstructed $\bar{\Lambda}$ candidates depending on p_T for different combinations of applied selection criteria on $\chi^2 \mathrm{geo_N DF}$ and $l/\Delta l$ divided by the signal-to-background ratio of the reconstructed particles without any selection.

(a) Efficiency distributions for the reconstructed Ξ^+ candidates.

(b) Efficiency of the reconstruction with different selection criteria divided by the reconstruction without any applied criteria.

(c) Signal-to-background ratio distributions for the reconstructed Ξ^+ candidates.

(d) Signal-to-background of the reconstruction with different selection criteria divided by the reconstruction without any applied criteria.

Figure 4.11: Efficiency and signal-to-background distributions for the reconstruction of Ξ^+ candidates depending on p_T for different selection criteria on $\chi^2_{\mathrm{geo}}/\mathrm{NDF}$ and $l/\Delta l$.

In both studies, for the reconstructed $\bar{\Lambda}$ and the Ξ^+ candidates, it is found that the efficiency and the signal-to-background ratio behave in the opposite way of each other, meaning that it is not possible to maximise the two quantities at the same time. Consequently, the type of the reconstruction and the analysed candidate sample has to be considered in order to choose the selection criteria in a reasonable way.

The reconstruction of the Ξ_c^0 baryon is the final goal of the analysis. This justifies the choice of the selection criteria on $\chi_{\mathrm{geo}}^2/\mathrm{NDF}$ and $l/\Delta l$ which are applied on the reconstructed Λ and Ξ candidates in the analysis of this thesis: $\chi_{\mathrm{geo}}^2/\mathrm{NDF}(\bar{\Lambda}) < 2$ and $\chi_{\mathrm{geo}}^2/\mathrm{NDF}(\Lambda) < 2$, $\chi_{\mathrm{geo}}^2/\mathrm{NDF}(\Xi^+) < 3$ and $\chi_{\mathrm{geo}}^2/\mathrm{NDF}(\Xi^-) < 3$, $l/\Delta l(\bar{\Lambda}) > 3$ and $l/\Delta l(\Lambda) > 3$, $l/\Delta l(\Xi^+) > 2$ and $l/\Delta l(\Xi^-) > 2$. They are chosen to increase the signal-to-background ratio in order to keep the particle sample clean for the reconstruction of the rare Ξ_c^0 signal.

4.3 Comparison of Variables

In the second part of the analysis the χ_{topo}^2 variable of Λ and Ξ candidates is examined together with the pointing angle (PA) θ of the according reconstructed particle pointing back to a certain vertex.

The PA is defined as the angle between the momentum vector of a reconstructed particle and the line connecting its decay vertex with the vertex that is considered to be the production vertex of the particle (see left hand side of Fig. 4.15). The cosine of the PA is commonly used as selection criterion to reject background candidates which are not pointing back to the assigned production vertex. This analysis aims to test the performance of the PA variable and compares it with the χ_{topo}^2 variable of the KF vertex fit.

4.3.1 χ_{topo}^2 Variable

The χ_{topo}^2 variable characterises the probability that a particle is produced in the region of the assigned production vertex. A candidate with a constraint set to the PV could for example be declared as secondary decay particle if the χ_{topo}^2 exceeds a certain value. The $\chi_{\mathrm{topo}}^2/\mathrm{NDF}$ distributions of Λ and Ξ candidates pointing back to the PV in real data and in MC have been compared and found to be consistent.

The distribution of $\chi_{\mathrm{topo}}^2/\mathrm{NDF}$ for $\bar{\Lambda}$ pointing back to the Ξ^+ decay vertex for signal
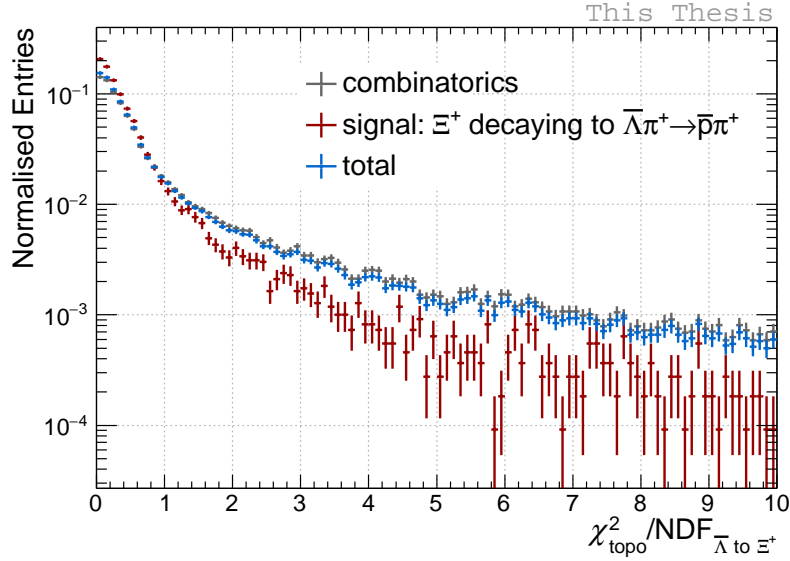
Figure 4.12: χ^2_{topo}/NDF distribution for $\bar{\Lambda}$ candidates pointing back to the reconstructed Ξ^+ decay vertex in MC, normalised to 1.

candidates and combinatorial background is shown in Fig. 4.12 respectively. The difference between the χ^2_{topo}/NDF signal and background distributions of the secondary $\bar{\Lambda}$ candidates at low values could be a possible indication that the variable can be used as selection criterion in order to separate signal and background. For the Ξ^+ candidates pointing back to the PV in Fig. 4.13, the signal distribution is peaked at small values of χ^2_{topo}/NDF due to the fact that the signal candidates usually have a good χ^2 value. The background distribution is flatter than the one for the signal in this case which could indicate that it is possible to use the variable as selection criterion in order to reject background candidates.

4.3.2 Pointing Angle

In order to compare the performance of the PA and χ^2_{topo} variables, the PA behaviour is investigated.

Fig. 4.14 shows the distributions of θ and $\cos\theta$ for the $\bar{\Lambda}$ candidates pointing back to the Ξ^+ decay vertex. The obtained results meet the expectation: in comparison with θ, the distribution of $\cos\theta$ is pushed to large or rather small values resulting in a steeper rise. The majority of the candidates are found to have small values of θ or large values of $\cos\theta$. Due to the limited detector resolution and the addition of the π^+ particle to the $\bar{\Lambda}$ candidate to reconstruct the Ξ^+ decay vertex, the distributions are broadened.
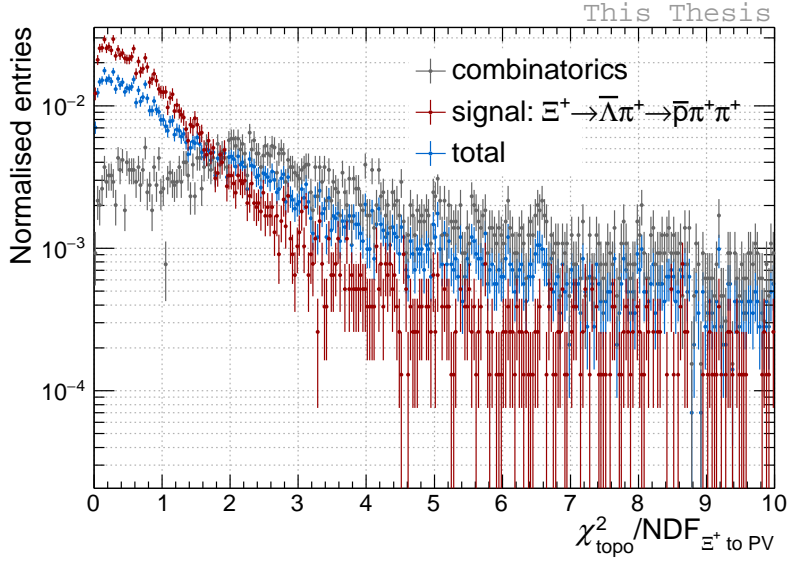
38

Figure 4.13: χ^2_{topo}/NDF distribution for Ξ^+ candidates pointing back to the PV in MC, normalised to 1.

However, also entries for θ near the value of π and negative values of $\cos\theta$ are found. This could be explained by a possibly wrong reconstruction of the $\bar{\Lambda}$ decay vertex. The vertex is reconstructed with a shorter distance to the PV than the Ξ^+ decay vertex (see Fig. 4.15) in this case. This leads to the fact that values of θ which are larger than $\frac{\pi}{2}$ are obtained.

In order to verify this hypothesis, the decay length of $\bar{\Lambda}$ candidates with negative as well as positive values of $\cos\theta$ is investigated and is shown in Fig. 4.16. The distribution supports the hypothesis of wrongly reconstructed $\bar{\Lambda}$ candidates. All particles with $\cos\theta < 0$ have a negative decay length, as their decay vertex lies within a shorter range of the PV than the Ξ^+ decay point. The number of these candidates is small compared to the number of particles with $\cos\theta > 0$ and a positive decay length. Therefore, they will not be taken into account.

Furthermore, the results for the analysis of the PA of Ξ^+ candidates pointing back to the PV are shown in Fig. 4.17. The signal behaves differently from the background in this case: the signal distribution is steeper for small and large values of the two observed variables. The combinatorial background distribution is flatter and in contrast to the $\bar{\Lambda}$ candidates pointing back to the Ξ^+ decay vertex, it drops for small and large values of θ (see Fig. 4.17a). This behaviour can also be observed for the signal candidates. The
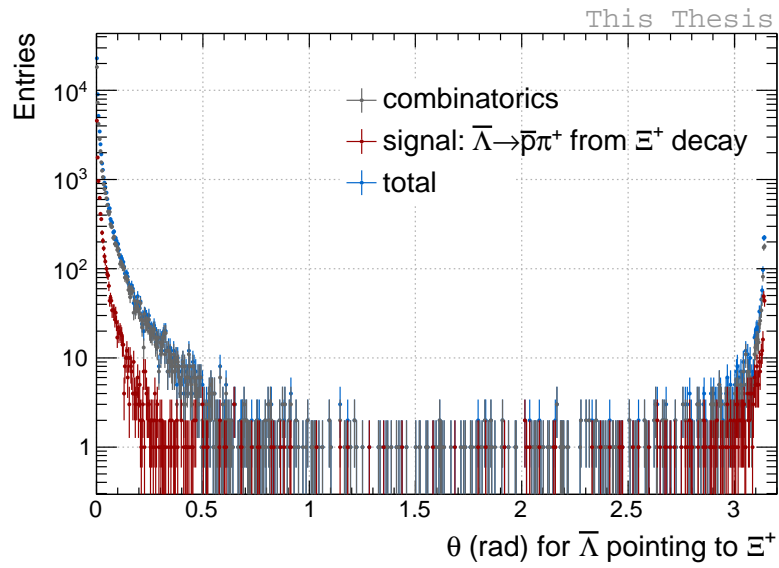
(a)
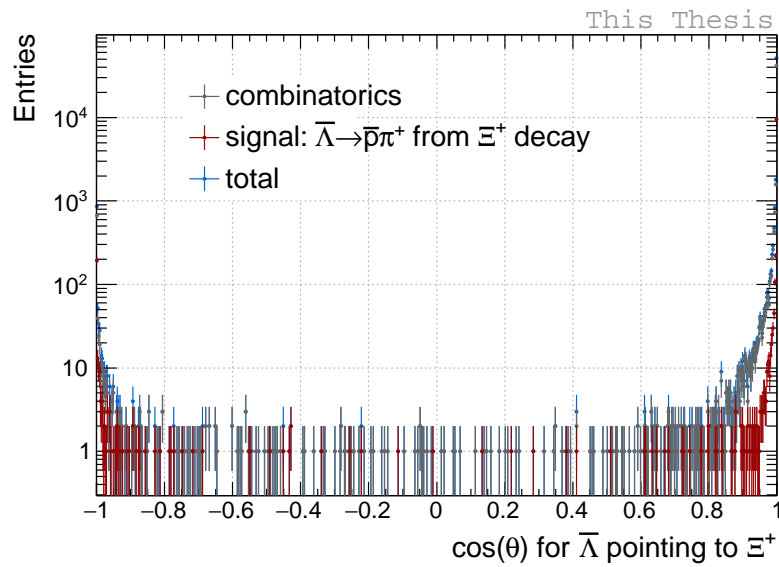
(b)

Figure 4.14: (a) PA distribution for $\bar{\Lambda}$ candidates pointing back to the reconstructed Ξ^+ decay vertex in MC (b) distribution of the cosine of the PA for $\bar{\Lambda}$ candidates pointing back to the reconstructed Ξ^+ decay vertex in MC.
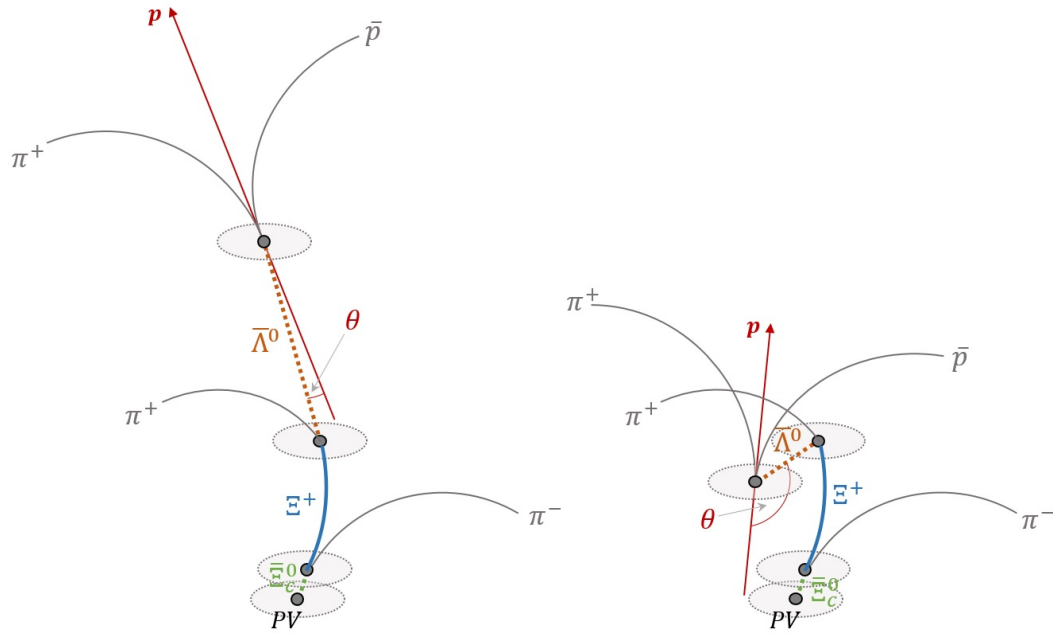
Figure 4.15: Proper $\bar{\Lambda}$ decay topology (left) and falsly reconstructed $\bar{\Lambda}$ decay vertex (right).
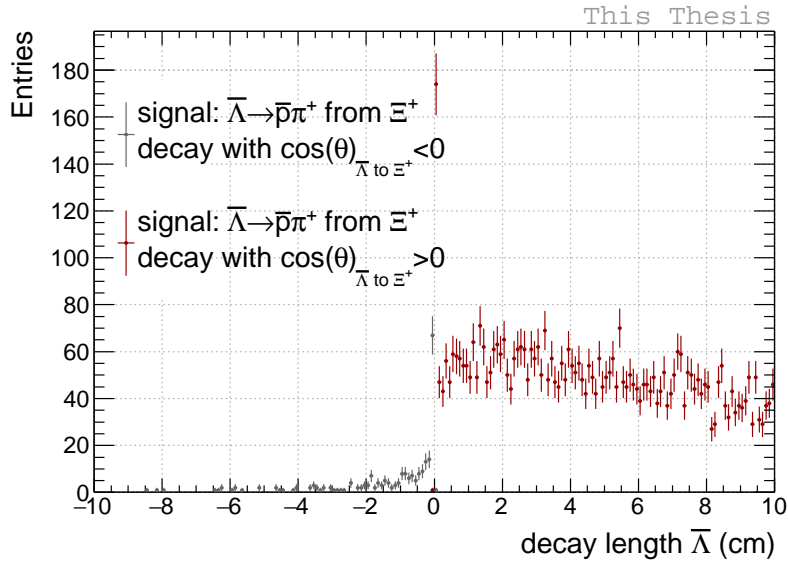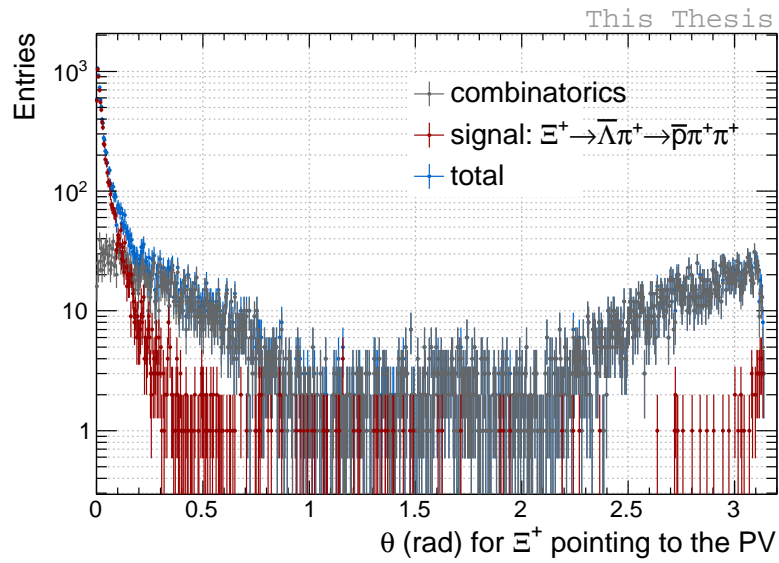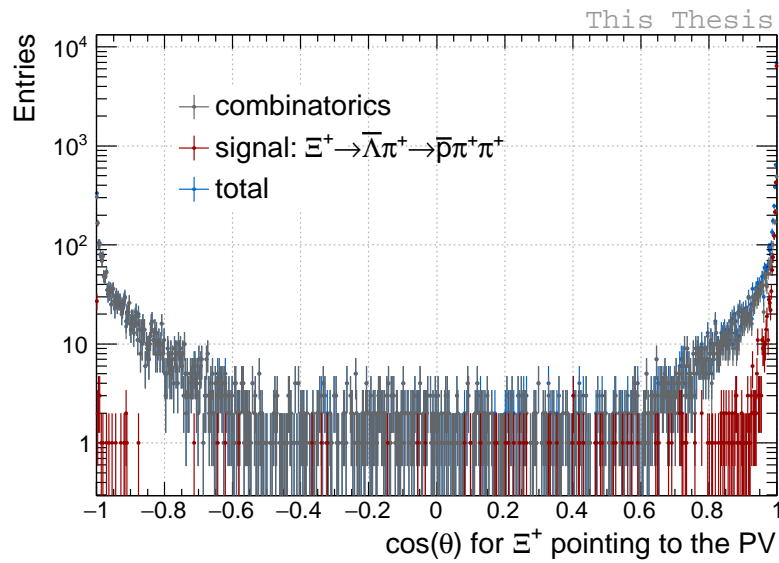

Figure 4.16: Distribution of the decay length of $\bar{\Lambda}$ candidates with $\cos\theta < 0$ and $\cos\theta > 0$ respectively.

(a)

(b)

Figure 4.17: (a) PA distribution for Ξ^+ candidates pointing back to the PV in MC (b) distribution of the cosine of the PA for Ξ^+ candidates pointing back to the PV in MC.

$\cos\theta$ distribution (see Fig. 4.17b) shows the same behaviour as for the $\bar{\Lambda}$ candidates as it is strongly shifted to $\cos\theta = 1$. Due to the flatter background distribution compared to the clear peak structure of the signal, the PA distribution of Ξ^+ pointing back to the PV inidcate clearly that it could be used to distinguish between signal and background candidates.

4.3.3 Comparison

In the last part of the analysis the performances of the PA and the χ^2_{topo} variables as selection criteria for the reconstruction of the $\bar{\Lambda}$ and Ξ^+ baryons are compared. Therefore, the efficiency of the reconstruction of the signal and background candidates depending on the value of the chosen selection criterion was examined respectively. Subsequently, the results for the PA, the cosine of the PA and the χ^2_{topo} variable were compared.

The signal efficiency (Eq. 4.5) is calculated as the ratio between the number of signal candidates that were reconstructed with an applied selection criterion and the number of reconstructed particles without a selection on the PA, the cosine of the PA or the $\chi^2_{\mathrm{topo}}/\mathrm{NDF}$. The same efficiency was calculated for the reconstructed background candidates (Eq. 4.6).

$$\epsilon_{rec}^{signal} = \frac{S_{rec}^{cut}}{S_{rec}} \tag{4.5}$$

$$\epsilon_{rec}^{background} = \frac{B_{rec}^{cut}}{B_{rec}} \tag{4.6}$$

Unlike the signal efficiency, which is aimed to be maximised, the background efficiency of the reconstruction should be as low as possible.

The results for the $\bar{\Lambda}$ candidates pointing back to the Ξ^+ decay vertex are shown in Fig. 4.18. The efficiency distributions for signal and background depending on a selection on the PA variable are rather similar, which can be seen in Fig. 4.18a. It is high for loose conditions and falls rapidly for very strong conditions on the PA. As expected, this behaviour is even more pronounced for the distributions corresponding to the cosine of the PA in Fig. 4.18b. Due to the fact that the background and signal efficiencies behave in a similar way, a clear statement whether the PA and its cosine are powerful selection tools for removing background candidates cannot be made from this distributions.
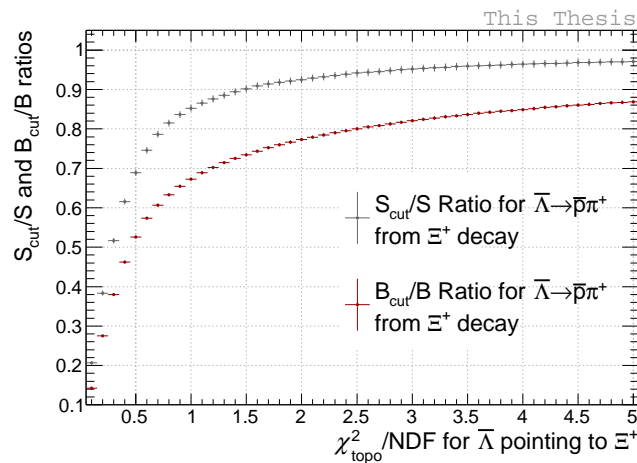
The reconstruction efficiency depending on different criteria on the $\chi^2_{\mathrm{topo}}/\mathrm{NDF}$ variable (shown in Fig. 4.18c) has a different behaviour. Even for loose selections on the KF
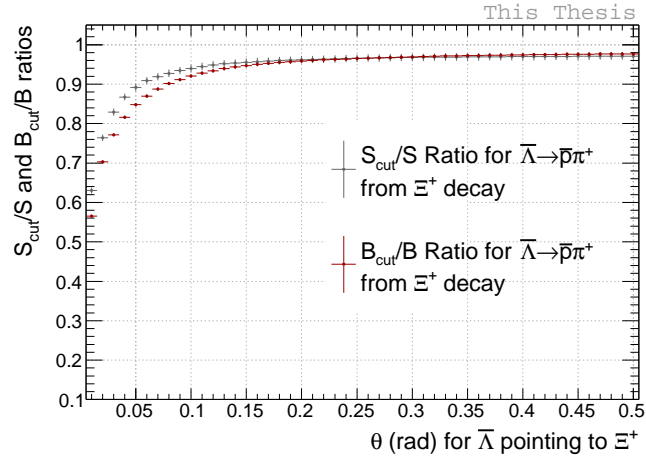
(a) Reconstruction efficiency of the PA as selection criterion.
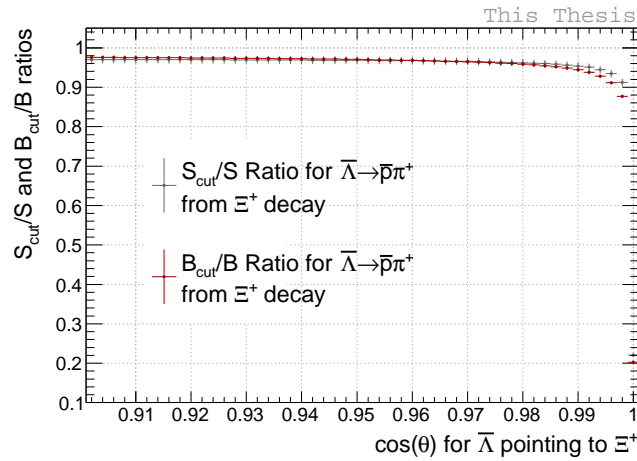
(b) Reconstruction efficiency of the cosine of the PA as selection criterion.

(c) Reconstruction efficiency of $\chi^2_{\text{topo}}/\text{NDF}$ as selection criterion.
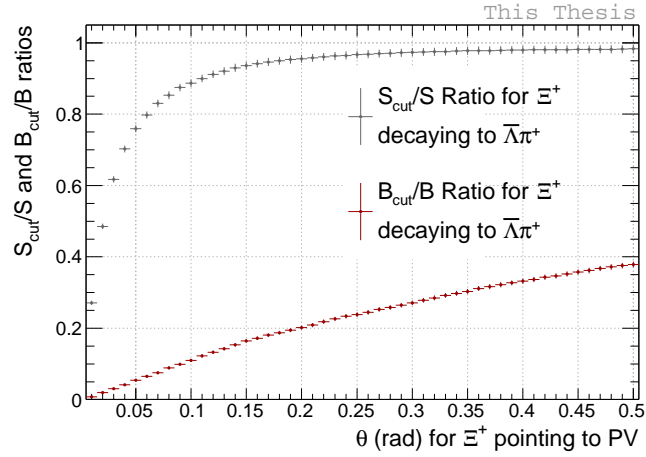
Figure 4.18: Signal and background efficiency distributions for the reconstruction of $\bar{\Lambda}$ candidates depending on the value of the according, applied selection criterion for $\bar{\Lambda}$ candidates pointing back to the reconstructed Ξ^+ decay vertex in MC.

variable the background efficiency is lower (smaller than 90%) than with selections on θ or $\cos\theta$, and at the same time the signal efficiency has a similar value as for loose conditions on these two variables, which is nearly 100%. As the signal efficiency should be maximised and the background efficiency minimised at the same time, the $\chi^2_{\text{topo}}/\text{NDF}$ variable could be a strong selection criterion in order to reject background and preserve signal in the case of the reconstructed $\bar{\Lambda}$ candidates.

The results of the analogue efficiency study on the Ξ^+ candidates pointing back to the PV are shown in Fig. 4.19. The plots show a different behaviour of the background. Again, the signal efficiency in Figs. 4.19a and 4.19b is high (nearly 100%) over a wide range of applied criteria on θ and $\cos\theta$. However, even for looser selections the background efficiency is smaller than 40%, meaning that even with low values of θ or $\cos\theta$ as selection criterion a high signal efficiency along with a low background efficiency can be achieved. This is not the case for the reconstruction with the KF variable $\chi^2_{\text{topo}}/\text{NDF}$ as a criterion. In Fig. 4.19c the signal efficiency for loose selections on $\chi^2_{\text{topo}}/\text{NDF}$ is about 90% and therefore worse than for conditions on θ or $\cos\theta$. Furthermore, the background efficiency is higher for the same loose selection.
Finally, the PA and its cosine of the Ξ^+ candidates pointing back to the PV seem to be more powerful variables in order to reject background than the KF variable χ^2_{topo}.

Therefore, the conclusion for the sudy on the reconstructed Ξ^+ candidates pointing back to the PV is opposite to the one for the $\bar{\Lambda}$ candidates pointing back to the Ξ^+ decay vertex. In the first case, the efficiency distributions (Fig. 4.19) indicate that the PA and its cosine are stronger tools for a particle selection, whereas in the second case the $\chi^2_{\text{topo}}/\text{NDF}$ variable (Fig. 4.18) shows a clearer distinction between signal and background distributions. The comparison of the different $\chi^2_{\text{topo}}/\text{NDF}$ distribtions could be one possibility to explain this discrepancy. In Fig. 4.20 the according distributions for $\bar{\Lambda}$ candidates pointing back to the Ξ^+ decay vertex, Ξ^+ particles pointing back to the PV, and $\bar{\Lambda}$ candidates pointing to the PV are shown. The two distributions with respect to the PV are flatter compared to the one of $\bar{\Lambda}$ pointing to the Ξ^+ decay vertex. The PV is reconstructed with the use of a variety of tracks, whereas the Ξ^+ decay vertex is reconstructed from just two tracks meaning that its localisation error is larger than the one of the PV. This leads to the fact that the $\chi^2_{\text{topo}}/\text{NDF}$ values with respect to the PV tend to be larger compared to the Ξ^+ decay vertex with a larger uncertainty on its localisation. This behaviour could be one explanation for the opposite conclusions of the two presented efficiency studies.

(a) Reconstruction efficiency of the PA as selection criterion.
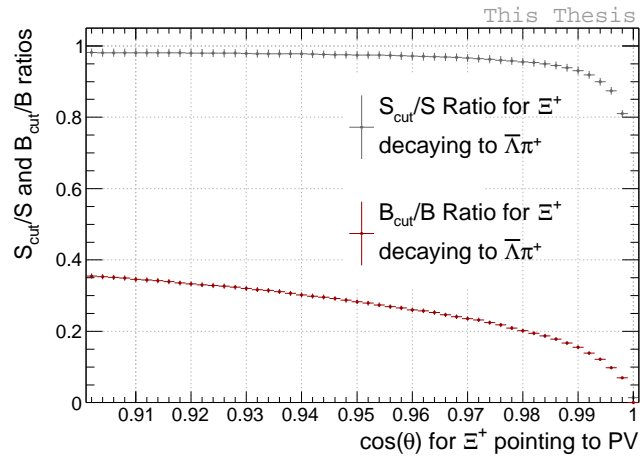
(b) Reconstruction efficiency of the cosine of the PA as selection criterion.
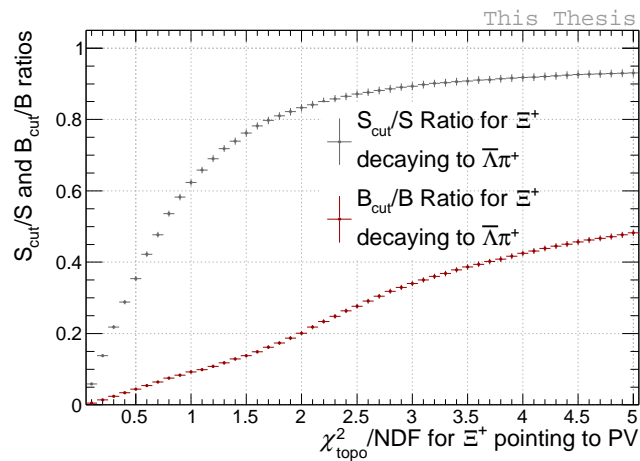
(c) Reconstruction efficiency of $\chi^2_{\text{topo}}/\text{NDF}$ as selection criterion.

Figure 4.19: Signal and background efficiency distributions for the reconstruction of Ξ^+ candidates depending on the value of the according, applied selection criterion for Ξ^+ candidates pointing back to the PV in MC.
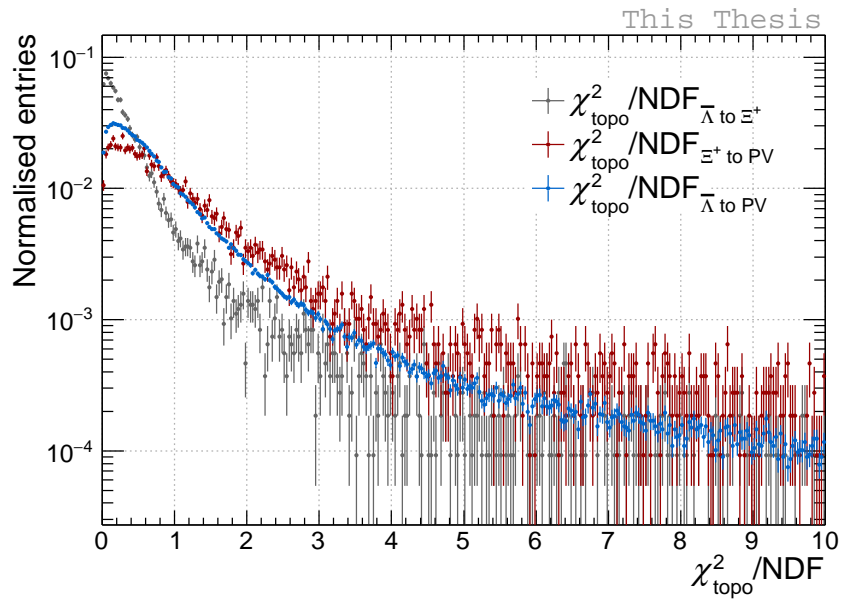
Figure 4.20: $\chi^2_{\text{topo}}/\text{NDF}$ distributions for the different indicated signal candidates, normalised to 1.

5 Conclusion and Outlook

The Ξ_c^0 baryon has been reconstructed via its hadronic decay in pp collisions at $\sqrt{s} = 5.02\,\text{TeV}$ for the first time with the ALICE detector. The KF Particle package for the reconstruction of complex decay topologies was used in order to test its performance within the ALICE framework. Several variables provided by the package were analysed in MC for the reconstruction of the Λ and Ξ hyperon candidates.

The investigated KF variables, χ^2_{geo}, $l/\Delta l$ and χ^2_{topo} behave in a reasonable way and can potentially be used as selection criteria in order to reject background or to distinguish between primary and secondary particle candidates. The reconstruction efficiency was found to amount to around 50-60% for the Λ and about 30% for the Ξ candidates. These results are comparable with traditional cascade reconstruction methods in ALICE.

The PA and the χ^2_{topo} were compared and it was found that they behave reasonably and can be used for a further selection on the Ξ_c^0 analysis. As additional input to the analysis the PA and the χ^2_{topo} of Λ candidates from Ξ_c^0 decays pointing back to the PV could be tested to find out if they can be used to reject primary Λ candidates.

The results show that the KF variables behave in a reasonably and, therefore, can be used in the analysis of charmed baryons. The reconstruction is comparable to common ALICE results. Hence, the KF Particle package is validated for the reconstruction of Λ and Ξ candidates from pp collisions at $\sqrt{s} = 5.02\,\text{TeV}$ in ALICE.

In order to optimise the reconstruction and selection of candidates, the background in real data has to be investigated. This will be one of the next steps in this analysis.

Furthermore, machine learning algorithms will be used in order to optimise the candidate selection and to further test and compare the performance of the different KF variables. In Fig. 5.1 the first results of this optimised study are shown. The invariant mass plot for the Ξ_c^0 candidates and their charge conjugates can be seen for two different p_{T}-intervals.

The objective of the full reconstruction of Ξ_c^0 baryons in ALICE was to contribute to the investigations of charm production and hadronisation in pp and in the presence of a QGP state. The study of the Ω_c^0 baryon via its decay to $\Omega^\mp \pi^\pm$ will be another possibility to learn more about charm production mechanisms in different collision systems.
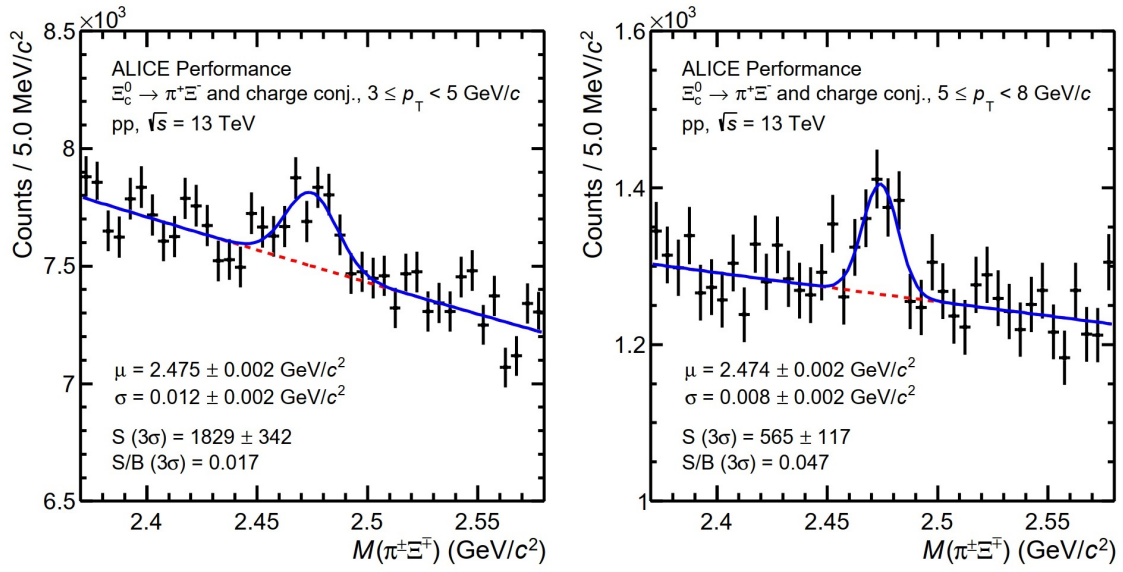
Figure 5.1: Invariant mass of Ξ_c^0 candidates reconstructed with the KF Particle package and an optimisation of the selection criteria using machine learning techniques.

List of Acronyms

ALICE A Large Ion Collider Experiment

CERN European Organisation for Nuclear Research

CMS Compact Muon Solenoid experiment

DCA distance of closest approach

DCal Di-Jet Calorimeter

EMCal Electromagnetic Calorimeter

HF heavy-flavour

HI heavy-ion

HMPID High Momentum Particle Identification Detector

IP interaction point

ITS Inner Tracking System

LHC Large Hadron Collider

LHCb Large Hadron Collider beauty experiment

MC Monte Carlo

MWPC multi-wire proportional chamber

p-Pb proton-lead

PA pointing angle

Pb-Pb lead-lead

PDF parton distribution function

PHOS Photon Spectrometer

PID particle identification

pp proton-proton

pQCD perturbative Quantum Chromodynamics

PS Proton Synchrotron

PV primary vertex

QCD quantum chromodynamics

QGP quark-gluon plasma

ROC Readout Chamber

SDD Silicon Drift Detectors

SM Standard Model of particle physics

SPD Silicon Pixel Detectors

List of Acronyms

SPS	Super Proton Synchrotron
SSD	Silicon Strip Detectors
TOF	Time-Of-Flight
TPC	Time Projection Chamber
TRD	Transition Radiation Detector
V0	VZERO

Bibliography

[1] *CERN Webpage*. 2019. URL: https://home.cern/science/physics/standard-model (visited on 11/12/2019).

[2] M. Tanabashi *et al.*, *Review of Particle Physics*. Phys. Rev. D **98** (2018), 030001. DOI: 10.1103/PhysRevD.98.030001.

[3] P. Braun-Munzinger and J. Wambach, *The Phase Diagram of Strongly Interacting Matter*. Rev. Mod. Phys. **81** (2009), 1031–1050.

[4] *FAIR-Center Webpage*. 2019. URL: https://fair-center.de/uploads/pics/sci_hadronic_matter_01.jpg (visited on 12/09/2019).

[5] A. K. Chadhuri, *A short Course on Relativistic Heavy Ion Collisions* (2012). eprint: arXiv:1207.7028v1[nucl-th]23Jul2012.

[6] H. Wang, *Study of Particle Ratio Fluctuations and Charge Balance Functions at RHIC*. PhD thesis. Michigan State University, 2018.

[7] J. Song, H. Li, and F. Shao, *New feature of low p_T charm quark hadronizstion in pp collisions at $\sqrt{s} = 7\,TeV$*. Eur. Phys. J C **78: 344** (2018). DOI: 10.1140/epjc/s10052-018-5817-x.

[8] ALICE collaboration, *First measurement of Ξ_c^0 production in pp collisions at $\sqrt{s} = 7\,TeV$*. Phys. Lett. B **781** (2018), 8–19. DOI: 10.1016/j.physletb.2018.03.061.

[9] ALICE collaboration, *Λ_c^+ production in pp collisions at $\sqrt{s} = 7\,TeV$ and in p-Pb collisions ar $\sqrt{s_{NN}} = 5.02\,TeV$*. JHEP **04** (2018), 108. DOI: 10.1007/JHEP04(2018)108.

[10] *CERN Webpage*. 2019. URL: https://home.cern/ (visited on 10/29/2019).

[11] L. Evans and P. Bryant, *LHC Machine*. JINST **3.08** (2008), S08001–S08001. DOI: 10.1088/1748-0221/3/08/s08001.

[12] *The CERN accelerator complex*. 2019. URL: https://cds.cern.ch/record/2197559 (visited on 10/08/2019).

[13] K. Aamodt *et al.*, *The ALICE experiment at the CERN LHC*. JINST **3** (2008), S08002. DOI: 10.1088/1748-0221/3/08/S08002.

[14] L. Betev *et al.*, *Definition of the ALICE Coordinate System and Basic Rules for Subdetector Components Numbering*. ALICE-INT-2003-038 (2003).

Bibliography

[15] F. Carminati *et al.*, *ALICE: Physics Performance Report, Volume I.* J. Phys. **G30** (2004), 1517–1763. DOI: 10.1088/0954-3899/30/11/001.

[16] J. Allen *et al.*, *ALICE DCal: An Addendum to the EMCal Technical Design Report Di-Jet and Hadron-Jet correlation measurements in ALICE.* In: 2010.

[17] *The ALICE Time Projection Chamber (TPC).* 2019. URL: http://aliceinfo.cern.ch/Public/en/Chapter2/Chap2_TPC.html (visited on 10/31/2019).

[18] J. Alme *et al.*, *The ALICE TPC, a large 3-dimensional tracking device with fast readout for ultra-high multiplicity events.* Nucl. Instr. and Meth. **A 622** (2010), 316–367. DOI: 10.1016/j.nima.2010.04.042.

[19] B. Abelev *et al.*, *Performance of the ALICE Experiment at the CERN LHC.* Int. J. Mod. Phys. **A29** (2014), 1430044. DOI: 10.1142/S0217751X14300440.

[20] T. Sjöstrand, S. Mrenna, and P. Skands, *PYTHA 6.4 Physics and Manual.* JHEP (2006). DOI: 10.1088/1126-6708/2006/05/026.

[21] R. Brun *et al.*, *GEANT Detector Description and Simulation Tool* (1994). DOI: 10.17181/CERN.MUHF.DMJ1.

[22] M. Zyzak, *Online selection of short-lived particles on many-core computer architectures in the CBM experiment at FAIR.* PhD thesis. Faculty of Computer Science and Mathematics Johann Wolfgang Goethe Uniersity Frankfurt am Main, 2015.

[23] S. Gorbunov and I. Kisel, *Reconstruction of decayed particles based on the Kalman filter.* CBM-SOFT-note-2007-003 (2007).

[24] S. Gorbunov, *On-line reconstruction algorithms for the CBM and ALICE experiments.* PhD thesis. Faculty of Computer Science and Mathematics Johann Wolfgang Goethe University Frankfurt, 2013.

Declaration of Authorship

Ich versichere, dass ich diese Arbeit selbstständig verfasst und keine anderen als die angegebenen Quellen und Hilfsmittel benutzt habe.

Heidelberg, den 11. Dezember 2019

Acknowledgements